Article

Demonstration of Silicon Nitride Optical Waveguide Parametric Amplifiers Integrated with Graphene Oxide Films

David Moss *

Posted Date: 2 May 2023

doi: 10.20944/preprints202305.0082.v1

Keywords: Third-order optical nonlinearity; 2D materials; telecommunications band; parametric amplifiers; graphene oxide; silicon nitride

Article

Demonstration of Silicon Nitride Optical Waveguide Parametric Amplifiers Integrated with Graphene Oxide Films

David J. Moss

Optical Sciences Centre, Swinburne University of Technology, Hawthorn, VIC 3122, Australia

Abstract: Optical parametric amplification (OPA) represents a powerful solution to achieve broadband amplification in wavelength ranges beyond the scope of conventional gain media, for generating high-power optical pulses, optical microcombs, entangled photon pairs and a wide range of other applications. Here, we demonstrate optical parametric amplifiers based on silicon nitride (Si_3N_4) waveguides integrated with two-dimensional (2D) layered graphene oxide (GO) films. We achieve precise control over the thickness, length, and position of the GO films using a transfer-free, layer-by-layer coating method combined with accurate window opening in the chip cladding using photolithography. Detailed OPA measurements with a pulsed pump for the fabricated devices with different GO film thicknesses and lengths show a maximum parametric gain of ~24.0 dB, representing a ~12.2 dB improvement relative to the device without GO. We perform a theoretical analysis of the device performance, achieving good agreement with experiment and showing that there is substantial room for further improvement. This work demonstrates a new way of achieving high photonic integrated OPA performance by incorporating 2D materials.

Keywords: integrated photonics; nonlinear optics; optical parametric process; 2D materials

Introduction

Optical amplifiers are key to many applications[1-3] such as optical communications where they have been instrumental with rare-earth-doped fibers[4-6] and III-V semiconductors[7-9]. However, these devices are restricted to specific wavelength ranges determined by the energy gaps between states[1,10]. In contrast, optical parametric amplification (OPA) can achieve gain across virtually any wavelength range[11,12], and so is capable of achieving broadband optical amplification outside of conventional wavelength windows[11,13]. Since its discovery in 1965[14], OPA has found applications in many fields such as ultrafast spectroscopy[15,16], optical communications[5,13], optical imaging[17,18], laser processing[19,20], and quantum optics[21,22]. Notably, it has underpinned many new technological breakthroughs such as optical microcombs[23,24] and entangled photon pairs[25,26].

To achieve OPA, materials with a high optical nonlinearity are needed – either second- ($\chi^{(2)}$) or third-order ($\chi^{(3)}$) nonlinearities[27,28], and has been demonstrated in birefringent crystals [29-31], optical fibers[10,32,33], and photonic integrated chips[1,3,24,34,35]. Amongst these, photonic integrated chips offer the advantages of a compact footprint, low power consumption, high stability and scalability, as well as cost reduction through large-scale manufacturing[36-38]. Despite silicon's dominance as a platform for linear photonic integrated devices[39,40], its significant two photon absorption (TPA) in the near infrared wavelength region and the resulting free carrier absorption lead to a high nonlinear loss[3,27], making it challenging to achieve any significant OPA gain in this wavelength range. Other nonlinear integrated material platforms, such as silicon nitride (Si_3N_4)[1,41], silicon rich nitride[42,43], doped silica[36,44], AlGaAs[45,46], chalcogenide[47,48], GaP[49], and tantala[50], exhibit much lower TPA at near infrared wavelengths and have made significant progress over the past decade. However, their comparatively low third-order optical nonlinearity imposes a significant limitation on the OPA gain that they can achieve.

Recently, two-dimensional (2D) materials with ultrahigh optical nonlinearities and broadband response have been integrated on photonic chips to achieve exceptional nonlinear optical

 doi:10.20944/preprints202305.0082.v1

performance[25,51-54], highlighted by the progress in realizing OPA by exploiting the high second-order optical nonlinearities of monolayer transition metal dichalcogenides (TMDCs)[25]. Previously[55-59], we reported an ultra-high third-order optical nonlinearity in 2D graphene oxide (GO) films that is about 4 orders of magnitude larger than silicon, together with a large bandgap (> 2 eV) that yields a linear loss more than 2 orders of magnitude lower than graphene, and perhaps most importantly, low TPA at near infrared wavelengths – all of which are key to achieving high OPA. In addition, GO has demonstrated high compatibility with various integrated platforms [12,38], along with the capability to achieve precise control over its film thickness and length[56,60].

In this work, we demonstrate significantly increased optical parametric gain in Si_3N_4 waveguides by integrating them with 2D layered GO films. We employ a transfer-free, layer-by-layer coating method to achieve precise control over the GO film thickness, and by using photolithography to open windows in the waveguide cladding we are able to accurately control the GO film length and position. We perform a detailed experimental characterization of the OPA performance of the devices with different GO film thicknesses and lengths, achieving a maximum parametric gain of ~24.0 dB, representing a ~12.2 dB improvement over the uncoated device. By fitting experimental results with theory, we analyse the influence of the applied power, wavelength detuning, and GO film thickness and length on the OPA performance, and in the process demonstrate that there is still significant potential for improved performance. These results verify the effectiveness of the on-chip integration of 2D GO films to improve the OPA performance of photonic integrated devices.

Experimental results

GO properties. Figure 1(a) illustrates the atomic structure and bandgap of GO, which is a derivative of graphene. Unlike graphene, which consists solely of sp^2-hybridized carbon atoms, GO contains various oxygen-containing functional groups (OCFGs) such as hydroxyl, carboxyl, and carbonyl groups[12]. Some of the carbon atoms in GO are sp^3-hybridized through σ-bonding with the OCFGs, resulting in a heterogeneous structure. In contrast to graphene, which has a zero bandgap, GO has an opened bandgap resulting from the isolated sp^2 domains within the sp^3 C–O matrix. The bandgap of GO typically falls between 2.1 eV and 3.6 eV[38], resulting in both low linear light absorption and low nonlinear TPA at near-infrared wavelengths that are attractive for nonlinear optical applications[54]. Moreover, the material properties of GO can be tuned by manipulating the OCFGs to engineer its bandgap, which has enabled a range of photonic, electronic, and optoelectronic applications[12].

Figure 1(b) illustrates the principle of signal amplification based on an optical parametric process[61]. In this process, when pump and idler photons travel collinearly through a nonlinear optical medium, a pump photon excites a virtual energy level. The decay of this energy level is stimulated by a signal photon, resulting in the emission of an identical second signal photon and an idler photon, while conserving both energy and momentum. In processes that involve optical absorption, such as photoluminescence and TPA, real photogenerated carriers are involved, which can alter the quiescent material nonlinear response[12,27]. In contrast, the optical parametric process operates by virtual excitation of carriers without creating photogenerated carriers. This makes it quasi-instantaneous, with ultrafast response times on the order of femtoseconds[1,54]. We note that although the parametric gain itself is almost instantaneous, when influenced by nonlinear absorption with much slower recovery times such as that induced by free carriers in silicon[27], the net parametric gain can accordingly have a slow time response component.

Preprints (www.preprints.org) | NOT PEER-REVIEWED | Posted: 2 May 2023 doi:10.20944/preprints202305.0082.v1

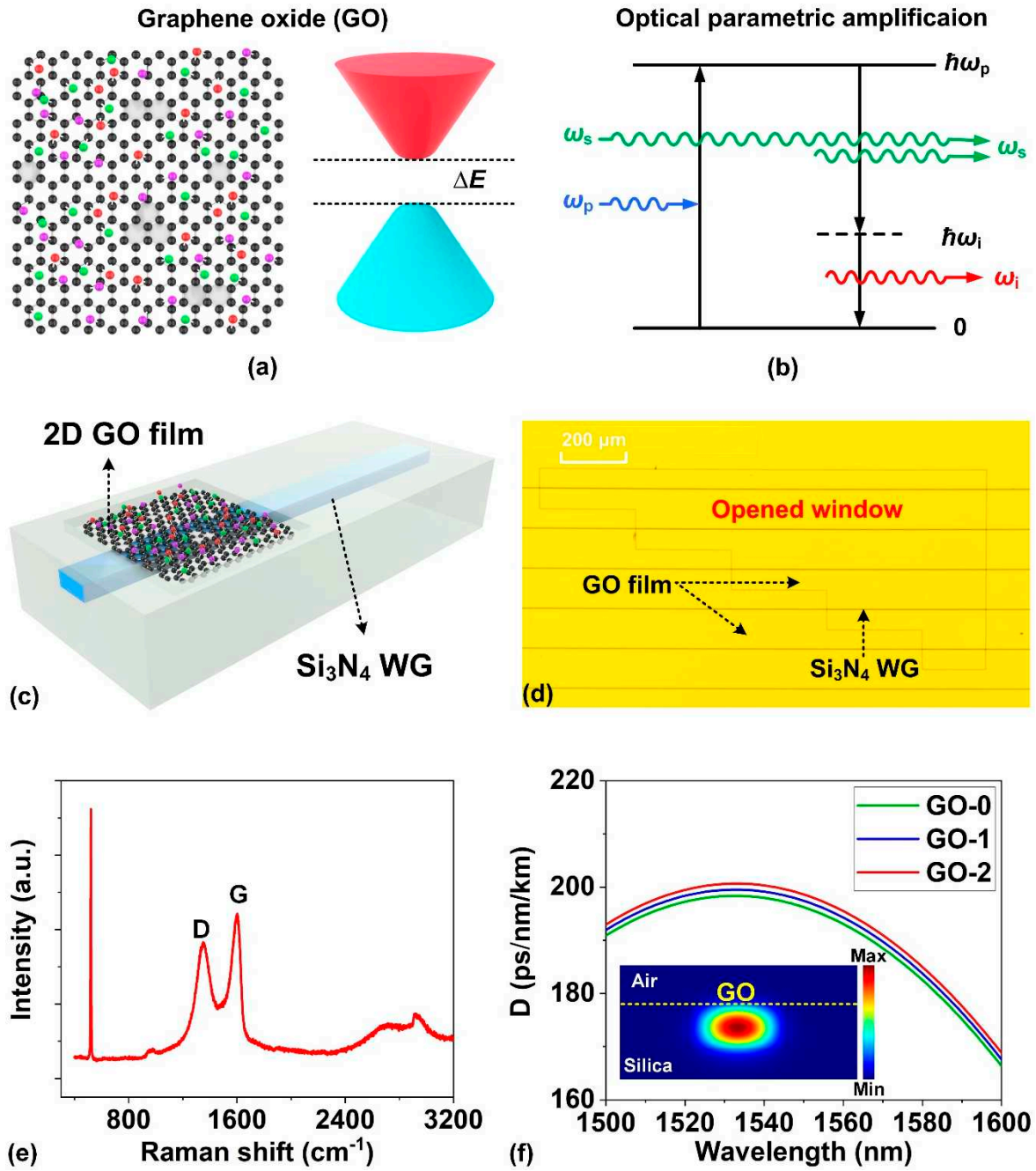

Figure 1. (a) Schematic of GO's atomic structure and bandgap. The colorful balls in the atomic structure represent the diverse oxygen-containing functional groups (OCFGs). (b) Schematic of signal amplification based on optical parametric process. (c) Schematic of a Si_3N_4 waveguide integrated with a single layer GO film. (d) Microscopic image of the fabricated Si_3N_4 integrated chip coated with a single layer GO film. (e) Measured Raman spectrum of the GO-coated Si_3N_4 chip in (d). (f) Dispersion (D) of the uncoated waveguide (GO-0) and hybrid waveguides with 1 and 2 layers of GO (GO-1, GO-2). Inset shows TE mode profile of the Si_3N_4 waveguide integrated with a single layer GO film.

Device design and fabrication. Figure 1(c) illustrates the schematic of a Si_3N_4 waveguide integrated with a single layer GO film. Compared to silicon that has a small (indirect) bandgap of ~1.1 eV[27], Si_3N_4 has a large bandgap of ~5.0 eV[36] that yields low TPA in the near-infrared region. To enable the interaction between the GO film and the evanescent field of the waveguide mode, a portion of the silica upper cladding was removed to allow for the GO film to be coated on the top surface of the Si_3N_4 waveguide. **Figure 1(d)** shows a microscopic image of the fabricated Si_3N_4 chip integrated with a single layer GO film. The successful coating of the GO film is confirmed by the presence of the

 doi:10.20944/preprints202305.0082.v1

representative D (1345 cm^{-1}) and G (1590 cm^{-1}) peaks in the measured Raman spectrum, as shown in **Figure 1(e)**. First, we fabricated low-loss Si_3N_4 waveguides via CMOS-compatible processes (see Methods). Next, we coated the waveguides with 2D GO films using a transfer-free, solution-based coating method (see Methods). This approach allows for large-area, layer-by-layer film coating with high repeatability and compatibility with various integrated material platforms[12,38,62]. The thickness of the GO film, characterized via atomic force microscopy measurements, was ~2 nm. The high transmittance and excellent morphology of the fabricated device demonstrate that our GO coating method, based on self-assembly via electrostatic attachment, can achieve conformal film coating in the window opening area without any noticeable wrinkling or stretching. This offers advantages compared to film transfer techniques commonly used for coating other 2D materials like graphene and TMDCs[19]. The length and position of the GO films can be easily controlled by adjusting the length and position of the windows opened on the silica upper cladding, which provides high flexibility for optimizing the performance of the hybrid waveguides by altering the GO film parameters.

Figure 1(f) shows the dispersion *D* of the uncoated waveguide and the hybrid waveguides with 1 and 2 layers of GO, calculated with commercial mode solving software using the materials' refractive indices measured by spectral ellipsometry. The Si_3N_4 waveguides in all these devices had a cross section of 1.60 μm × 0.72 μm, and the inset in **Figure 1(f)** depicts the transverse electric (TE) mode profile of the hybrid waveguide with 1 layer of GO. The interaction between the highly nonlinear GO film and the waveguide's evanescent field enhances the nonlinear optical response of the hybrid waveguide, which is the foundation for improving the OPA performance. We selected TE-polarization for our subsequent measurements since it supports in-plane interaction between the waveguide's evanescent field and the GO film, which is much stronger than the out-of-plane interaction due to the significant optical anisotropy in 2D materials[63,64]. In **Figure 1(f)**, it can be observed that all three waveguides exhibit anomalous dispersion, which is crucial for reducing phase mismatch and improving the parametric gain in the optical parametric process. Upon incorporating 1 layer of GO, the hybrid waveguide shows a slightly increased anomalous dispersion compared to waveguides without GO. For the hybrid waveguides with 2 layers of GO, the anomalous dispersion is further enhanced.

Loss measurements. The coating of GO films onto Si_3N_4 waveguides introduces extra linear and nonlinear loss. Before the OPA measurements, we used the experimental setup in **Figure S1** of the Supplementary Information to characterize the linear and nonlinear loss of the fabricated devices. Fiber-to-chip coupling was achieved via lensed fibers butt coupled to inverse-taper couplers at both ends of the Si_3N_4 waveguides. The coupling loss was ~4.2 dB / facet. We measured three devices, including the uncoated Si_3N_4 waveguide and hybrid waveguides with 1 and 2 layers of GO. The Si_3N_4 waveguides in these devices were all ~20 mm in length, while for the hybrid waveguides, windows with a length of ~1.4 mm were opened at a distance of ~0.7 mm from the input port. In our following discussion, the input light power quoted refers to the power coupled into the devices, with the fiber-to-chip coupling loss being excluded.

The linear loss was measured using continuous-wave (CW) light with a power of ~1 mW. **Figure 2a** shows the insertion loss of the fabricated devices versus wavelength. All devices exhibited nearly a flat spectral response, which suggests the absence of any material absorption or coupling loss that would generate a strong wavelength dependence. By using a cut-back method[65], we obtained a propagation loss of ~0.5 dB/cm for the Si_3N_4 waveguides buried in silica cladding. By comparing the Si_3N_4 waveguides with and without opened windows in the silica cladding, we deduced a higher propagation loss of ~3.0 dB/cm for the Si_3N_4 waveguides in the opened window area, which can be attributed to the mitigating effect of the silica cladding on the Si_3N_4 surface roughness. Finally, using these values and the measured insertion loss of the hybrid waveguides, we extracted an excess propagation loss induced by the GO films of ~3.1 dB/cm and ~6.3 dB/cm for the 1- and 2-layer devices, respectively. Such a loss induced by the GO films is about 2 orders of magnitude lower than Si_3N_4 waveguides integrated with graphene films[66,67], which can be attributed to the large bandgap of GO, resulting in low light absorption at near infrared wavelengths. This is a crucial advantage of GO in OPA applications where low loss is required to achieve a high net parametric gain.

Preprints (www.preprints.org) | NOT PEER-REVIEWED | Posted: 2 May 2023 doi:10.20944/preprints202305.0082.v1

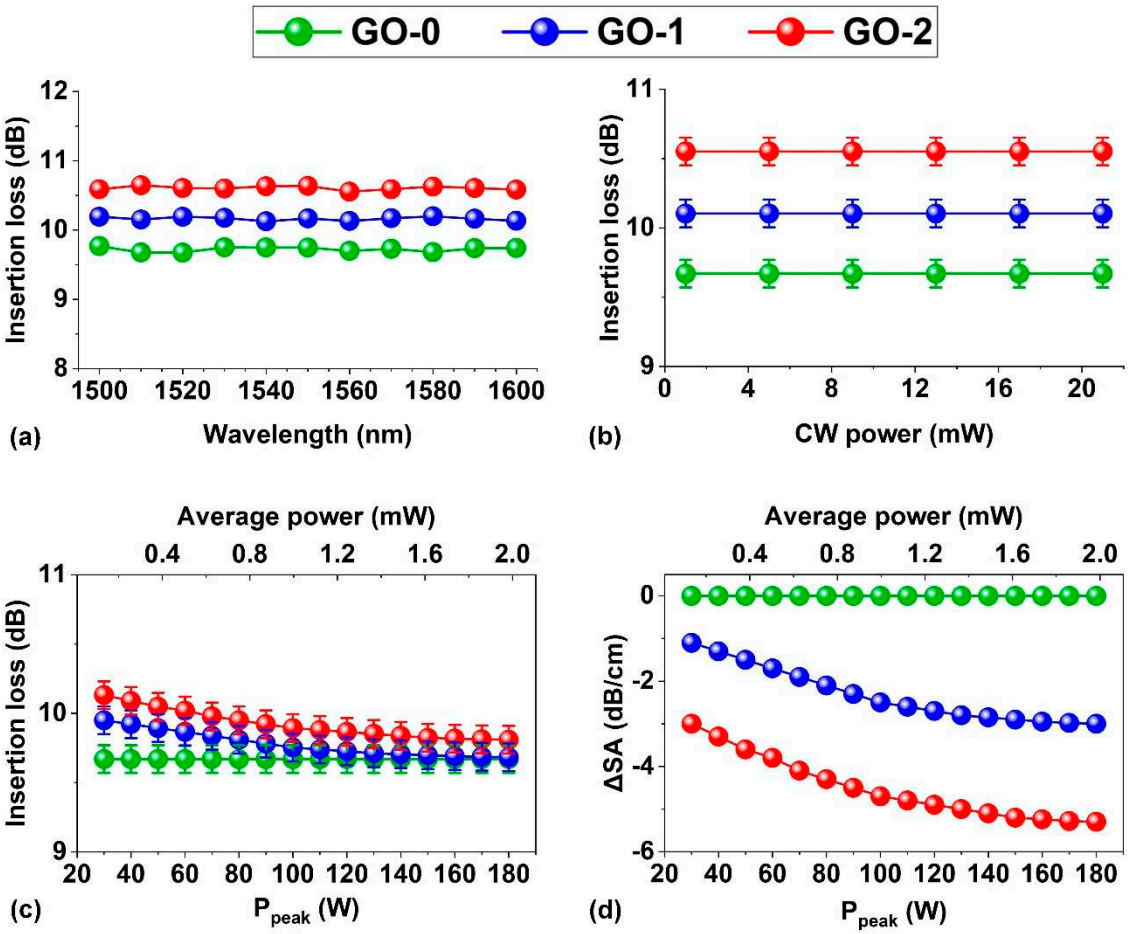

Figure 2. Experimental results for loss measurements. (a) Measured insertion loss versus wavelength of input continuous-wave (CW) light. The input CW power is ~1 mW. (b) Measured insertion loss versus input CW power. The input CW wavelength is ~1550 nm. (c) Measured insertion loss versus peak power P_{peak} of 180-fs optical pulses. (d) Excess propagation loss induced by SA of GO ΔSA versus P_{peak} extracted from (c). In (a) – (d), the curves for GO-0, GO-1, and GO-2 show the results for the uncoated Si_3N_4 waveguides, and the hybrid waveguides with 1 and 2 layers of GO, respectively.

Figure 2b shows the measured insertion loss versus input CW power at a wavelength of ~1550 nm. All devices showed no significant variation in insertion loss when the power was below 30 mW, indicating that the power-dependent loss induced by photo-thermal changes in the GO films was negligible within this range. This observation is consistent with our previous results where photo-thermal changes were only observed for average powers above 40 mW[56,68].

The measurement of nonlinear loss was conducted using a fiber pulsed laser (FPL) capable of generating nearly Fourier-transform limited femtosecond optical pulses centered around 1557 nm. The pulse duration and repetition rate were ~180 fs and ~60 MHz, respectively. **Figure 2c** shows the measured insertion loss versus pulse peak power P_{peak}. The average power of the femtosecond optical pulses was adjusted using a variable optical attenuator, ranging from 0.32 mW to 1.94 mW, which corresponds to peak powers ranging from 30 W to 180 W. The insertion loss of the hybrid waveguides decreased as the pulse peak power increased, with the 2-layer device exhibiting a more significant decrease than the 1-layer device. In contrast, the insertion loss of the uncoated Si_3N_4 waveguide remained constant. These results reflect that the hybrid waveguides experienced saturable absorption (SA) in the GO films, consistent with observations in waveguides incorporating graphene[66,69]. Additionally, we note that the loss changes observed were not present when using CW light with equivalent average powers. This suggests that the changes are specifically induced by optical pulses with high peak powers. In GO, the SA can be induced by the bleaching of the ground states that are associated with sp^2 orbitals (e.g., with an energy gap of ~0.5 eV[55]) as well as the defect states. **Figure**

Preprints (www.preprints.org) | NOT PEER-REVIEWED | Posted: 2 May 2023 doi:10.20944/preprints202305.0082.v1

2d shows the SA-induced excess propagation loss (ΔSA) versus pulse peak power P_{peak}, which was extracted from the result in **Figure 2c,** with the linear propagation loss being excluded. The negative values of ΔSA indicate that there is a decrease in loss as the peak power increases in the SA process. Such decrease in loss is beneficial for increasing the pump peak power in the OPA process, which helps improve the parametric gain.

OPA experiments. We conducted OPA experiments using the same devices that were fabricated and used for the loss measurements. A schematic of the experimental setup is shown in **Figure 3**. To generate the pump light required for the OPA experiments, we employed the same FPL that was used for the loss measurements. On the other hand, the signal light was generated through amplification of the CW light from a tunable laser. The pulsed pump and the CW signal were combined by a broadband 50:50 coupler and sent to the device under test (DUT) for the optical parametric process. The polarization of both signals was adjusted to TE polarized using two polarization controllers (PCs). To adjust the power of the pulsed pump, a broadband variable optical attenuator (VOA) was utilized. The output after propagation through the DUT was directed towards an optical spectrum analyzer (OSA) for analysis.

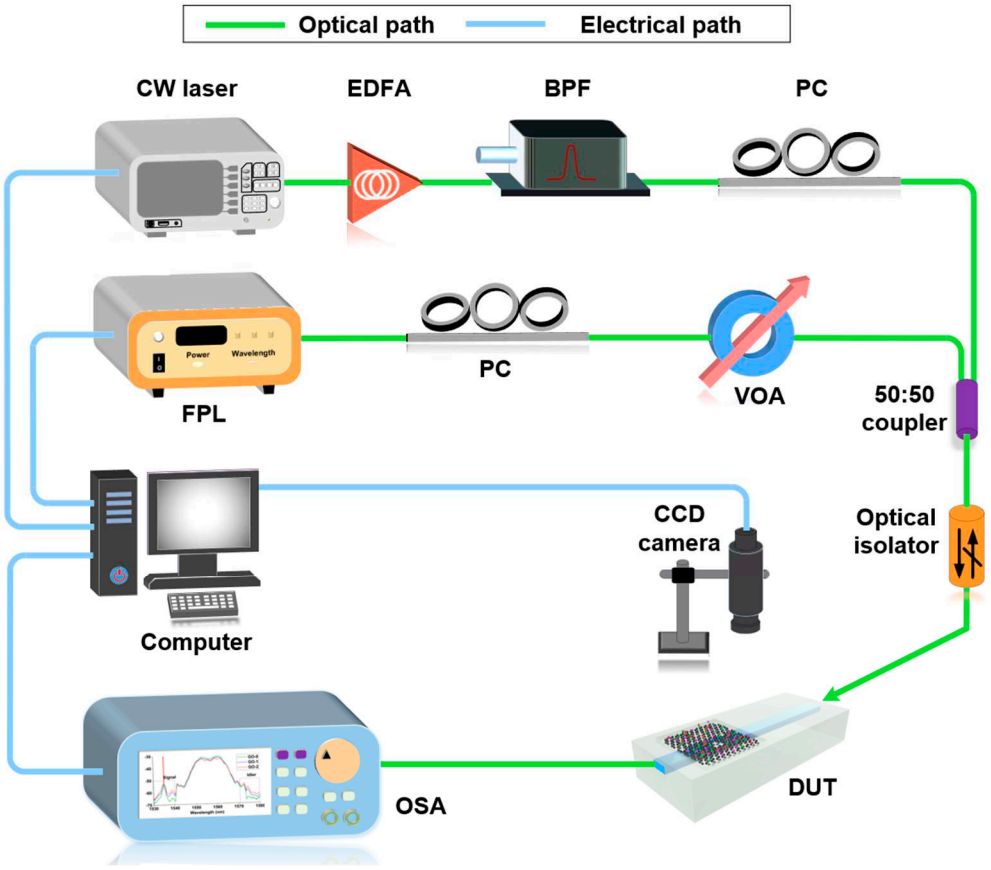

Figure 3. Experimental setup for OPA experiments. CW laser: continuous-wave laser. FPL: fiber pulsed laser. PC: polarization controller. EDFA: Erbium doped fiber amplifier. VOA: variable optical attenuator. OPM: optical power meter. DUT: device under test. CCD: charged-coupled device. OSA: optical spectrum analyzer.

Figure 4a shows the optical spectra after propagation through the uncoated Si_3N_4 waveguide and the hybrid waveguides with 1 and 2 layers of GO. For all three devices, the input pump peak power and signal power were kept the same at P_{peak} = ~180 W and P_{signal} = ~6 mW, respectively. As the pump light used for the OPA experiments was pulsed, the optical parametric process occurred at a rate equivalent to the repetition rate of the FPL. As a result, both the generated idler and amplified signal also exhibited a pulsed nature with the same repetition rate as that of the FPL. The optical spectra in **Figure 4a** were analyzed to extract the parametric gain PG experienced by the signal light

Preprints (www.preprints.org) | NOT PEER-REVIEWED | Posted: 2 May 2023 doi:10.20944/preprints202305.0082.v1

for the three devices (see Methods). The *PG* for the uncoated Si_3N_4 waveguide and the hybrid waveguides with 1 and 2 layers of GO were ~11.8 dB, ~20.4 dB, and ~24.0 dB, respectively. The hybrid waveguides exhibited higher parametric gain compared to the uncoated waveguide, and the 2-layer device had higher parametric gain than the 1-layer device. These results confirm the improved OPA performance in the Si_3N_4 waveguide by integrating it with 2D GO films. We also note that the hybrid devices showed greater spectral broadening of the pulsed pump caused by self-phase modulation (SPM), which is consistent with our previous observations from SPM experiments[57].

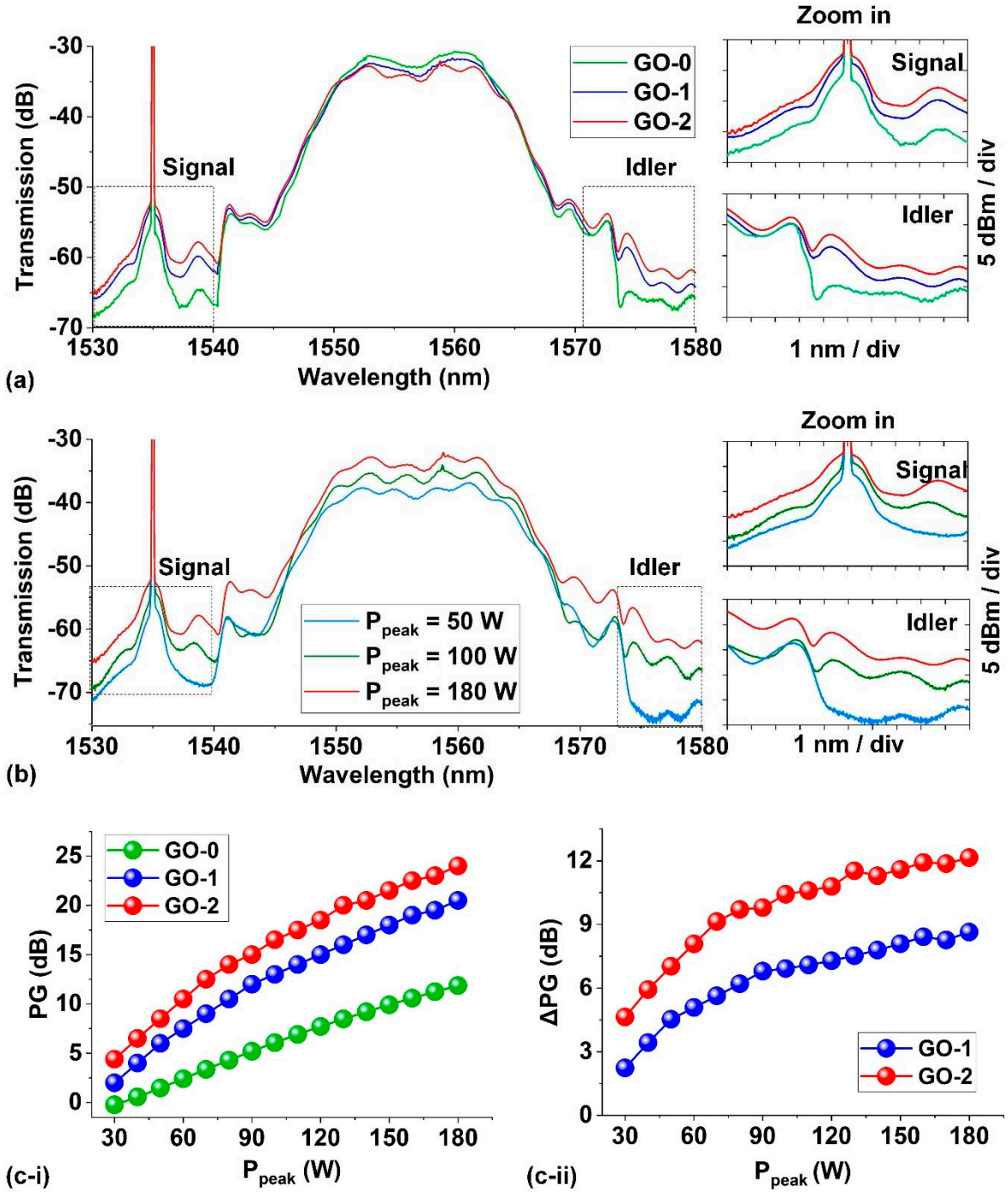

Figure 4. Optical parametric amplification (OPA) using a 180-fs pulsed pump and a continuous-wave (CW) signal. (a) Measured output optical spectra after propagation through uncoated (GO-0) and hybrid waveguides with 1 (GO-1) and 2 (GO-2) layers of GO. The peak power of the input pump light P_{peak} was ~180 W. (b) Measured output optical spectra after propagation through the device with 2 layers of GO at different P_{peak}. In (a) and (b), the power of the CW signal light was P_{signal} = ~6 mW, and

 doi:10.20944/preprints202305.0082.v1

insets show zoom-in views around the signal and idler. (c) Measured (i) parametric gain *PG* and (ii) parametric gain improvement *ΔPG* versus P_{peak}. .

The values of *PG* in **Figure 4** are the net parametric gain, over and above the waveguide loss induced by both the GO-coated and uncoated Si_3N_4 waveguide segments (see Methods). This is different to the "on/off" parametric gain often quoted [11,43], where the waveguide loss is excluded, resulting in higher values of parametric gain. Here, the on-off gains for the waveguides with 0, 1, and 2 layers of GO were ~13. 2 dB, ~22.3 dB, and ~26.2 dB, respectively, which are only slightly higher than their corresponding net gains due to the low loss of the Si_3N_4 waveguides and the relatively short GO film length. Although the net gain can be increased closer to the on-off gain by reducing the waveguide loss via optimization of the fabrication processes, because the differences between the net and on-off gains are small in our case, there is not much incentive to do this. In the following, we focus our discussion on the net parametric gain *PG*. This can also ensure a fair comparison of the parametric gain improvement, as different waveguides have different waveguide loss.

Figure 4b shows the measured output optical spectra after propagation through the device with 2 layers of GO for different P_{peak}. **Figure 4c-i** shows the signal parametric gain *PG* for the uncoated and hybrid waveguides versus input pump peak power, and the parametric gain improvement *ΔPG* for the hybrid waveguides as compared to the uncoated waveguide is further extracted and shown in **Figure 4c-ii**. We varied the input pump peak power from ~30 W to ~180 W, which corresponds to the same power range used in **Figure 2d** for loss measurements. The *PG* is higher for the hybrid waveguide with 1 layer of GO compared to the uncoated waveguide, and lower than the device with 2 layers of GO. In addition, both *PG* and *ΔPG* increase with P_{peak}, and a maximum *ΔPG* of ~12.2 dB was achieved for the 2-layer device at P_{peak} = ~180 W. Likewise, we observed similar phenomena when using lower-peak-power picosecond optical pulses for the pump, as shown in **Figure S2** of the Supplementary Information.

To evaluate the OPA performance, we conducted experiments where we varied the wavelength detuning, CW signal power, and GO film length. Except for the varied parameters, all other parameters are the same as those in **Figure 4**. In **Figure 5a**, the measured signal parametric gain *PG* and parametric gain improvement *ΔPG* are plotted against the wavelength detuning $\Delta\lambda$, which is defined as the difference between the CW signal wavelength λ_{signal} and the pump center wavelength λ_{pump}. It is observed that both the *PG* and *ΔPG* increase as $\Delta\lambda$ changes from -12 nm to -22 nm. In **Figure 5b**, the *PG* and *ΔPG* are plotted against the CW signal power P_{signal}, showing a slight decrease as P_{signal} increases, which is primarily due to the fact that an increase in P_{signal} can result in a decrease in *PG* as per its definition (i.e., $PG = P_{out,signal} / P_{in,signal}$, see Methods). **Figure 5c** shows the *PG* and *ΔPG* versus GO film length. By measuring devices with various GO film lengths, ranging from ~0.2 mm to ~1.4 mm, we observed that those with longer GO films exhibited greater *PG* and *ΔPG* values. The *PG* achieved through the optical parametric process is influenced by several factors, such as the applied powers, optical nonlinearity, dispersion, and loss of the waveguides. These factors will be comprehensively analyzed in the following section.

Preprints (www.preprints.org) | NOT PEER-REVIEWED | Posted: 2 May 2023 doi:10.20944/preprints202305.0082.v1

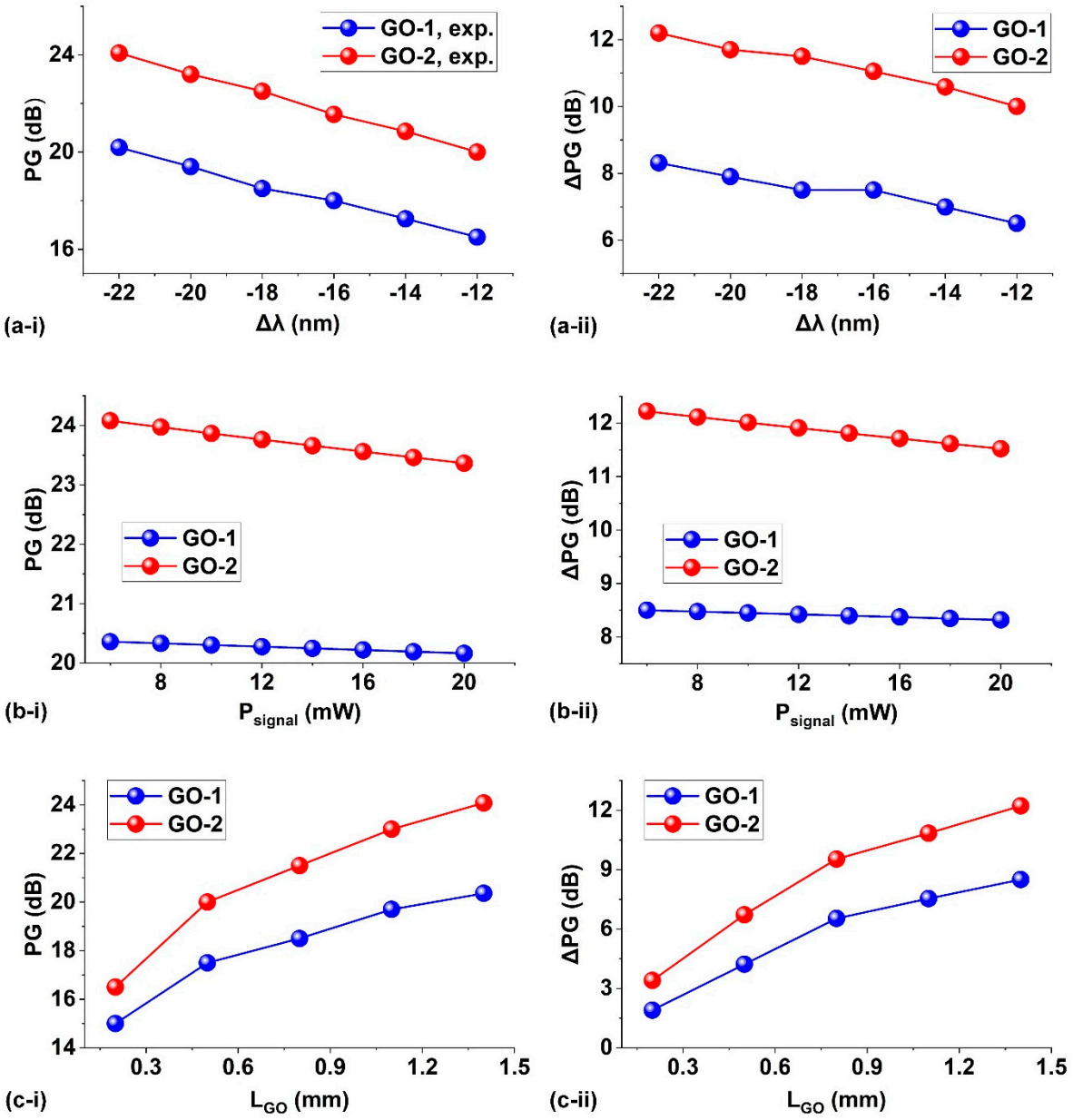

Figure 5. (a) Measured (i) parametric gain *PG* and (ii) parametric gain improvement *ΔPG* versus wavelength detuning $\Delta\lambda$. (b) Measured (i) *PG* and (ii) *ΔPG* versus input CW signal power P_{signal}. (c) Measured (i) *PG* and (ii) *ΔPG* versus GO film length L_{GO}. In (a) – (c), the peak power of the 180-fs pulsed pump centered around 1557 nm was P_{peak} = ~180 W. Except for the varied parameters, all other parameters are kept the same as $\Delta\lambda$ = ~-22 nm, P_{signal} = ~6 mW, and L_{GO} = ~1.4 mm.

Analysis and discussion

Optical nonlinearity of hybrid waveguides and GO films. We used the theory from Refs.[10,58,70] to model the OPA process in the fabricated devices (see Methods). By fitting the measured *PG* with theory, we obtained the nonlinear parameter γ of the uncoated and hybrid waveguides. The fit γ for the uncoated Si_3N_4 waveguide is ~1.11 $W^{-1}m^{-1}$, which is consistent with the previously reported values in the literature[58,71-82]. **Figure 6a** shows the fit γ of the hybrid waveguides as a function of pulse peak power P_{peak}. For both devices with different GO film thickness, the lack of any significant variation in γ with P_{peak} indicates that the applied power has a negligible effect on the properties of the GO films. This is in contrast to the effects of light with high average optical powers, which can lead to changes in GO's properties via photo-thermal reduction[56,58]. The fit values of γ for the devices with 1 and 2 layers of GO are ~14.5 and ~27.3 times greater than the value for the uncoated Si_3N_4 waveguide.

Preprints (www.preprints.org) | NOT PEER-REVIEWED | Posted: 2 May 2023 doi:10.20944/preprints202305.0082.v1

These agree with our earlier work[58,59] and indicate a significant improvement in Kerr nonlinearity for the hybrid waveguides.

Based on the fit γ for the hybrid waveguides, we further extracted the Kerr coefficient n_2 of the GO films (see Methods), as shown in **Figure 6b**. The extracted n_2 values for the films with 1 and 2 layers are similar, with the former being slightly higher than the latter. The lower n_2 for thicker films is likely caused by an increase in inhomogeneous defects within the GO layers and imperfect contact between multiple GO layers. The n_2 values for the films with 1 and 2 layers are about 5 orders of magnitude higher than that of Si_3N_4 (~2.62×10^{-19} m^2/W, obtained by fitting the result for the uncoated Si_3N_4 waveguide), highlighting the tremendous third-order optical nonlinearity of the GO films.

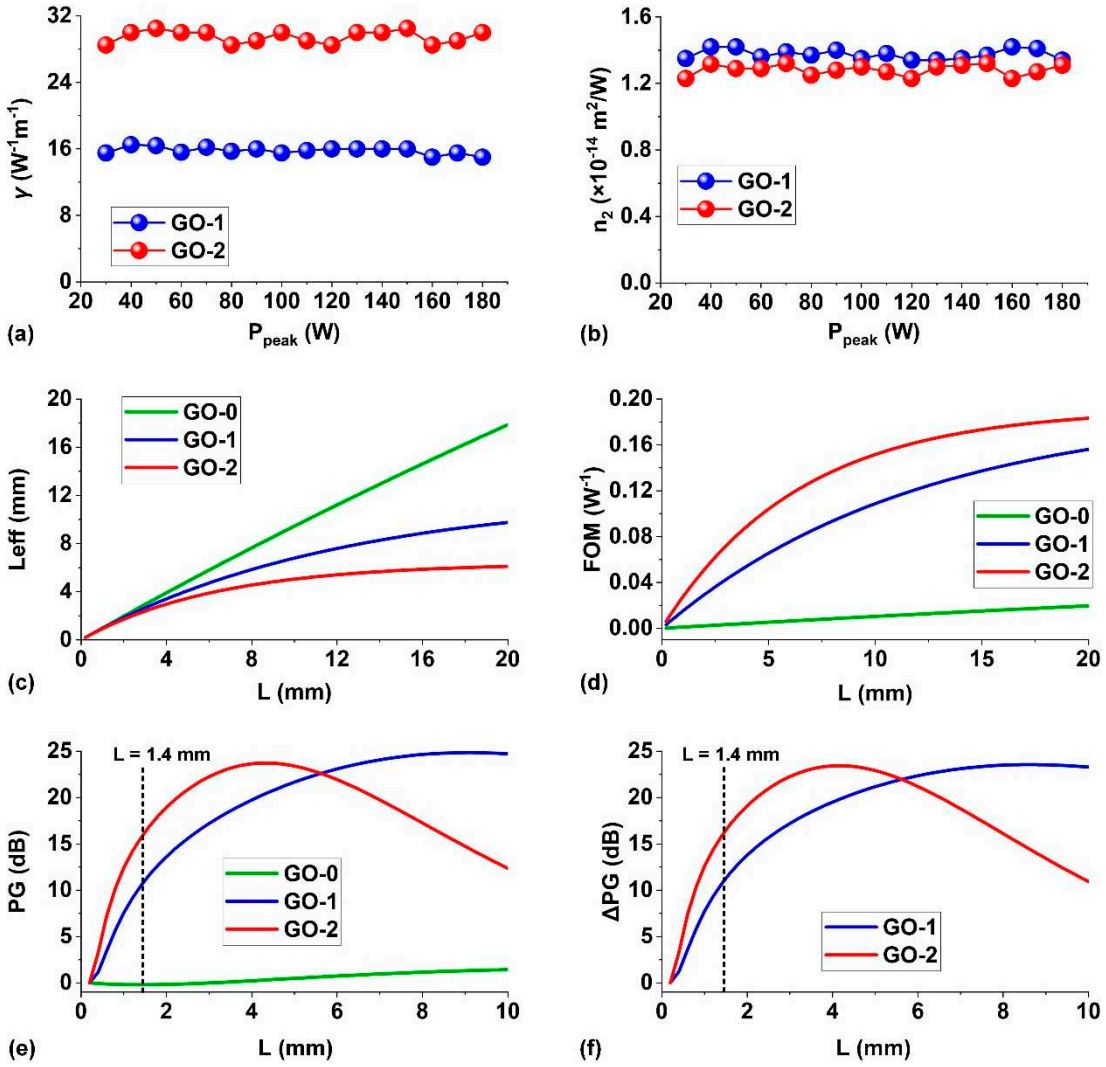

Figure 6. (a) Nonlinear parameter γ of hybrid waveguides with 1 (GO-1) and 2 (GO-2) layers of GO as a function of pump peak power P_{peak}. (b) Kerr coefficient n_2 of films with 1 (GO-1) and 2 (GO-2) layers of GO versus P_{peak}. (c) Effective interaction length L_{eff} and (d) figure of merit FOM versus waveguide length L for the uncoated (GO-0) and hybrid waveguides with 1 (GO-1) and 2 (GO-2) layers of GO. (e) Parametric gain PG and (f) parametric gain improvement ΔPG versus waveguide length L for the uncoated Si_3N_4 waveguide (GO-0) and the hybrid waveguides uniformly coated with 1 (GO-1) and 2 (GO-2) layers of GO. In (e) and (f), the pump peak power, CW signal power, and the wavelength detuning are P_{peak} = ~180 W, P_{signal} = ~6 mW, and $\Delta\lambda$ = ~-22 nm, respectively.

We also quantitatively compare the nonlinear optical performance of the Si_3N_4 waveguide and the hybrid waveguides by calculating their nonlinear figure of merit FOM. The FOM is determined by balancing a waveguide's nonlinear parameter against its linear propagation loss, and can be expressed as a function of waveguide length L given by:

Preprints (www.preprints.org) | NOT PEER-REVIEWED | Posted: 2 May 2023 doi:10.20944/preprints202305.0082.v1

$$FOM\ (L) = \gamma \times L_{eff}\ (L) \quad (1)$$

where γ is the waveguide nonlinear parameter and $L_{eff}\ (L) = [1 - exp\ (-\alpha \times L)]\ /\alpha$ is the effective interaction length, with α denoting the linear loss attenuation coefficient. Note that the nonlinear figure of merit defined in **Eq. (1)** allows for comparison of the nonlinear optical performance of optical waveguides made from different materials. This is distinct from the nonlinear figure of merit commonly used for comparing the nonlinear optical performance of a single material, which is defined as $n_2/(\lambda \cdot \beta_{TPA})$[36], with n_2, λ, and β_{TPA} denoting the Kerr coefficient, wavelength, TPA coefficient, respectively.

Figure 6c shows L_{eff} versus L for the Si_3N_4 waveguide and the hybrid waveguides with 1 and 2 layers of GO. The Si_3N_4 waveguide has a higher L_{eff} due to its comparably lower linear propagation loss. **Figure 6d** shows the *FOM* versus L for the three waveguides. Despite having a lower L_{eff}, the hybrid waveguides exhibit a higher *FOM* than the Si_3N_4 waveguide, owing to the significantly improved nonlinear parameter γ for the hybrid waveguides. This indicates that the impact of enhancing the optical nonlinearity is much greater than the degradation caused by the increase in loss, resulting in a significant improvement in the device's overall nonlinear optical performance.

For the hybrid waveguides that we measured in the OPA experiments, only a specific section of the waveguides was coated with GO films. In **Figures 6e** and **6f,** we compare *PG* and ΔPG versus waveguide length L for the hybrid waveguides uniformly coated with GO films, respectively, which were calculated based on the fit γ values (at P_{peak} = ~180 W) in **Figure 6a**. The pump peak power, CW signal power, and wavelength detuning were P_{peak} = ~180 W, P_{signal} = ~6 mW, and $\Delta\lambda$ = ~-22 nm, respectively – the same as those in **Figure 4a**. The corresponding results for the uncoated Si_3N_4 waveguide are also shown for comparison. The 2-layer device has higher *PG* and ΔPG values for L < ~5.7 mm but lower values for L > ~5.7 mm, reflecting the trade-off between the increase in optical nonlinearity and waveguide loss. At L = 1.4 mm, the 1-layer and 2-layer devices achieve *PG* of ~10.5 dB and ~15.6 dB, respectively. When compared to waveguides that have patterned GO films of the same length as those used in our OPA experiments, their total *PG* (including those provided by both the ~1.4-mm-long GO-coated section and the ~18.6-mm-long uncoated section) are ~20.4 dB and ~24.0 dB, respectively. This highlights the dominant role of the GO-coated section in providing the parametric gain, as well as the fact that a further improvement in ΔPG could be obtained by increasing the length of the GO-coated segments.

Performance improvement by optimizing parameters. Based on the OPA modeling (see Methods) and the fit parameters in **Figure 6**, we further investigate the margin for performance improvement by optimizing the parameters.

Figure 7a shows the calculated *PG* for the hybrid waveguides versus pulse peak power P_{peak} and CW signal power P_{signal}. The corresponding results for ΔPG are shown in **Figure 7b**. In each figure, (i) and (ii) show the results for the devices with 1 and 2 layers of GO, respectively. The black points mark the experimental results in **Figure 4**, and the black crossings mark the results corresponding to the maximum values of *PG* or ΔPG. As can be seen, both *PG* and ΔPG increase with P_{peak} but decrease with P_{signal}, showing agreement with the trends observed in the experimental results. For the device with 1 layer of GO, the maximum *PG* of ~32.7 dB and ΔPG of ~10.7 dB are achieved at P_{peak} = 400 W and P_{signal} = 1 mW. Whereas for the device with 2 layers of GO, the maximum *PG* and ΔPG are ~36.9 dB and ~15.0 dB at the same P_{peak} and P_{signal}, respectively. This reflects that there is a large room for improvement by further optimizing the pulse peak power and the CW signal power. In our experiments, the maximum output power of our FPL limited the applied pulse peak power. In addition, we opted to avoid using excessively low CW signal power due to two reasons. First, the CW signal power does not exert a significant influence on PG. Second, as the power of the output pulsed signal diminishes with the decrease of the input CW signal power, it becomes increasingly challenging to extract *PG* accurately.

Preprints (www.preprints.org) | NOT PEER-REVIEWED | Posted: 2 May 2023 doi:10.20944/preprints202305.0082.v1

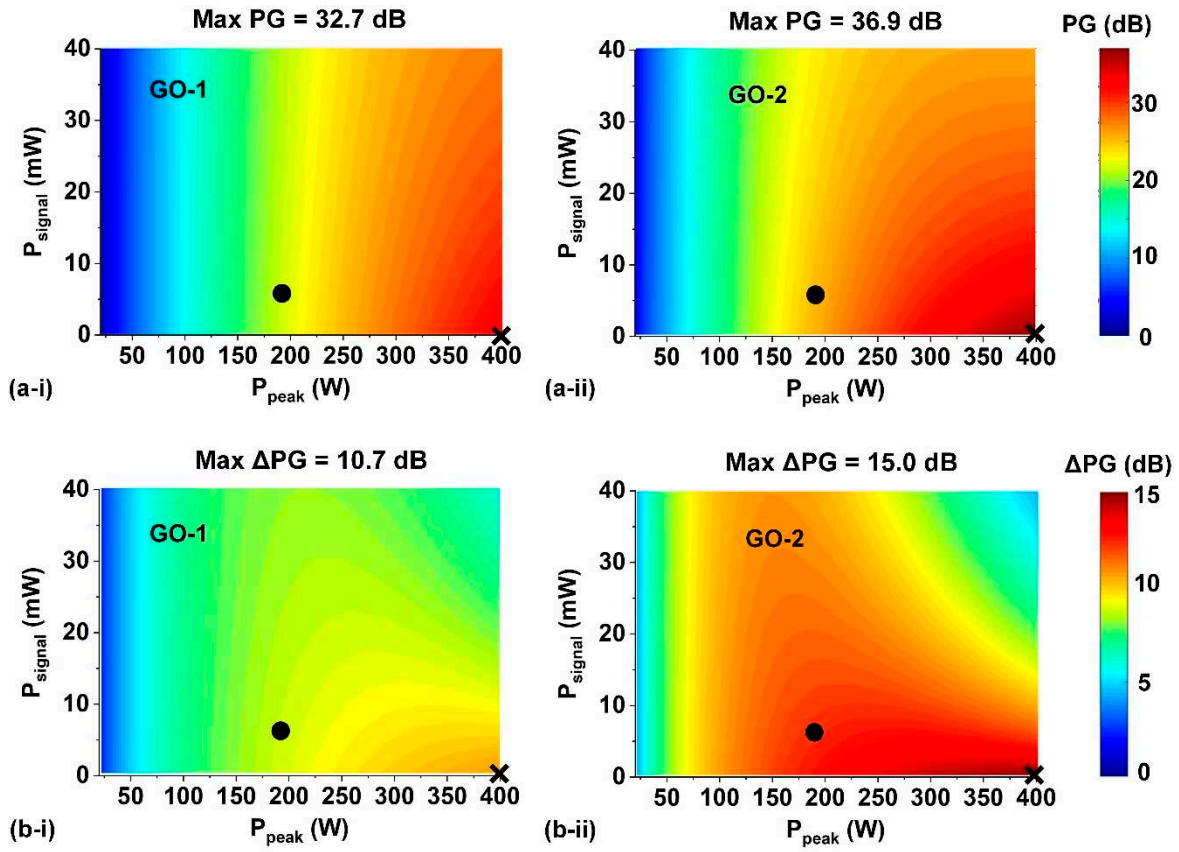

Figure 7. (a) Simulated parametric gain *PG* versus input pump peak power P_{peak} and CW signal power P_{signal}. (b) Simulated parametric gain improvement Δ*PG* versus P_{peak} and P_{signal}. In (a) and (b), (i) and (ii) show the results for the hybrid waveguides with 1 and 2 layers of GO (GO-1, GO-2), respectively. The black points mark the OPA experimental results, and the black crossing mark the results corresponding to the maximum values of *PG* and Δ*PG*. The wavelength detuning and the GO film length are $\Delta\lambda$ = -22 nm and L_{GO} = 1.4 mm, respectively.

Figure 8a shows the calculated *PG* and Δ*PG* versus wavelength detuning $\Delta\lambda$. The dashed curves were calculated based on the fit result at $\Delta\lambda$ = -22 nm, and the data points mark the measured results in **Figure 5a**. The curves with an 'M' shape are consistent with the results in Refs.[3,10,11], reflecting the anomalous dispersion of these waveguides. The experimental data points match closely with the simulation curves, thereby confirming the consistency between our experimental results and theory. For the device with 1 layer of GO, the maximum *PG* of ~34.7 dB and Δ*PG* of ~14.7 dB are achieved at $\Delta\lambda$ = ~-67 nm and ~-80 nm, respectively. Whereas for the 2-layer device, the maximum *PG* of ~37.6 dB and Δ*PG* of ~17.3 dB are achieved at $\Delta\lambda$ = ~-61.8 nm and ~-57.8 nm, respectively. These results highlight the significant potential for improvement through further optimization of the wavelength detuning. In our experiments, the range of wavelength detuning was limited by the operation bandwidth of the erbium-doped fiber amplifier used to amplify the CW signal power.

Preprints (www.preprints.org) | NOT PEER-REVIEWED | Posted: 2 May 2023 doi:10.20944/preprints202305.0082.v1

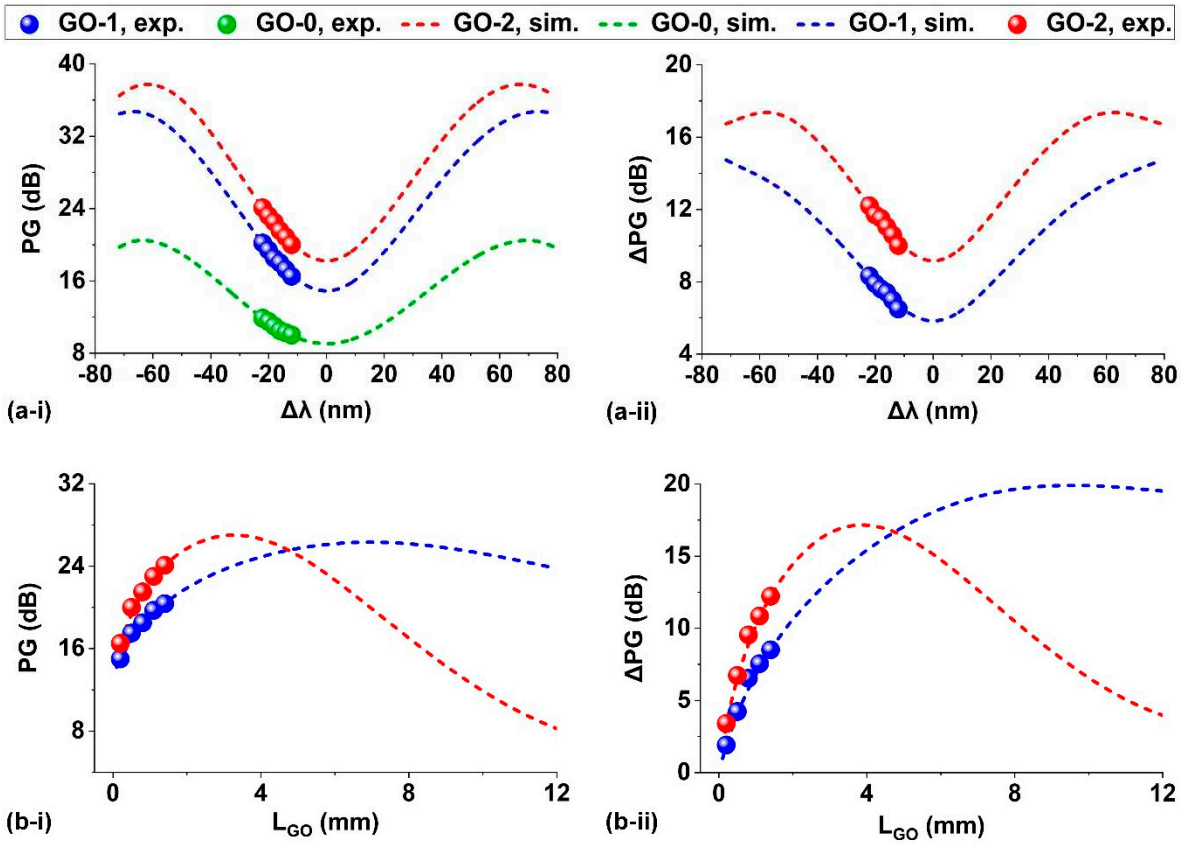

Figure 8. (a) Simulated (i) parametric gain *PG* and (ii) parametric gain improvement Δ*PG* versus wavelength detuning $\Delta\lambda$. (b) Simulated (i) *PG* and (ii) Δ*PG* versus GO coating length L_{GO}. In (a) and (b), the measured and fit results are shown by the data points and the dashed curves, respectively. The pump peak power and the signal power are P_{peak} = 180 W and P_{signal} = 6 mW, respectively. In (a), L_{GO} = 1.4 mm. In (b), $\Delta\lambda$ = -22 nm.

We also investigate the performance improvement by optimizing the GO film length L_{GO}. **Figure 8b** shows the calculated *PG* and Δ*PG* versus L_{GO}. The dashed curves were calculated based on the fit result at L_{GO} = 1.4 mm, and the data points mark the measured results in **Figure 5a**. For the device with 1 layer of GO, the maximum *PG* of ~26.3 dB and Δ*PG* of ~19.9 dB are achieved at L_{GO} = ~7 mm and ~9.7 mm, respectively. Whereas for the device with 2 layers of GO, the maximum *PG* of ~27.0 dB and Δ*PG* of ~17.2 dB are achieved at L_{GO} = ~3.3 mm and ~3.9 mm, respectively. These results suggest that the OPA performance can be improved by further optimizing the length of the GO film. In our experiments, the lengths of the GO films were restricted by the size of the opened windows on the silica cladding (as shown in **Figure 1d**). Aside from optimizing the GO film length, we would anticipate even higher values of *PG* and ΔPG for devices with an increased number of GO layers at L_{GO} = 1.4 mm, similar to what we observed in our previous nonlinear optics experiments[56,57]. This is due to the considerably increased optical nonlinearity of devices with thicker GO films. However, such an increase in optical nonlinearity is accompanied by a rise in loss, making it imperative to balance the trade-off between them.

We investigate the performance by optimizing both $\Delta\lambda$ and L_{GO} simultaneously (see **Figure S4** of the Supplementary Information), finding that the 1-layer device has a maximum *PG* of ~37.4 dB and maximum Δ*PG* of ~31.5 dB, while the 2-layer device reaches *PG* up to ~37.8 dB and Δ*PG* up to ~27.3 dB. In addition, by further increasing the pump peak power from 180 W to 400 W, even higher performance is achieved, with the 1-layer device reaching a maximum *PG* of ~43.7 dB and maximum Δ*PG* of ~40.1 dB, and the 2-layer device a maximum *PG* of ~43.8 dB and maximum Δ*PG* of ~37.3 dB (see **Figure S5** of the Supplementary Information). According to these simulation results, it is found that if both $\Delta\lambda$ and L_{GO} are optimized simultaneously, there is not much difference between the

Preprints (www.preprints.org) | NOT PEER-REVIEWED | Posted: 2 May 2023 doi:10.20944/preprints202305.0082.v1

maximum *PG* for the 1- and 2- layer devices. However, the 1-layer device still yields a slightly higher Δ*PG* because of its lower loss compared with the 2-layer device. For this reason, devices coated with more GO layers will have lower maximum Δ*PG*.

Finally, we also investigate the improvement in *PG* and Δ*PG* by optimizing the coating position of the GO films (see **Figure S6** of the Supplementary Information), as well as the influence of the SA of GO on the OPA performance (see **Figure S7** of the Supplementary Information). We find that although optimizing the coating position can lead to further improvements in *PG* and Δ*PG*, the extent of these improvements is not as substantial as those achieved through optimization of $\Delta\lambda$ and L_{GO}. In addition, we find that the SA of GO has a positive impact on enhancing *PG* and Δ*PG*, especially for devices with thicker GO films. These results have significant implications for devices involving microcombs[83-138] that require high on-chip parametric gain, as well as linear, nonlinear [139-158] and potentially quantum[159-170] optical chips.

Conclusion

In summary, we experimentally demonstrate significantly improved OPA performance in Si_3N_4 waveguides integrated with 2D GO films compared to uncoated waveguides. We fabricate GO-Si_3N_4 hybrid waveguides with precise control of the thickness, length, and position of the GO films. Detailed OPA measurements are performed for the fabricated devices using a pulsed pump and CW signal. The results show that up to ~24.0 dB parametric gain is achieved for the hybrid devices, representing a ~12.2 dB improvement relative to the device without GO. Based on the experimental results, the influence of the pump / signal power, wavelength detuning, and GO film thickness / length on the OPA performance is theoretically analyzed, showing that further improvement can be achieved by optimizing these parameters. We calculate that a parametric gain of ~37.8 dB and a parametric gain improvement of ~31.5 dB should be possible by optimizing the wavelength detuning and GO film length, and even higher to 43.8 dB by increasing the pump peak power to 400 W. Our study provides valuable insights into the promising potential of on-chip integration of 2D GO films for enhancing the OPA performance of photonic integrated devices, of benefit to many nonlinear optical applications.

Materials and methods

Fabrication of Si_3N_4 waveguides. The Si_3N_4 waveguides were fabricated via CMOS compatible processes[72]. First, a Si_3N_4 film was deposited on a silicon wafer with a 3-μm-thick wet oxidation layer on its top surface, using a low-pressure chemical vapor deposition (LPCVD) method. The deposition was carried out in two steps involving a twist-and-grow process, resulting in a crack-free film. Next, waveguides were created using 248-nm deep ultraviolet lithography followed by fluorocarbon-based dry etching with $CF_4/CHF_3/Ar$, which resulted in a low sidewall surface roughness for the waveguides. After waveguide patterning, we employed a multi-step, chemical-physical, in-situ annealing sequence using H_2, O_2, and N_2 to further reduce the loss of the Si_3N_4 waveguides. Subsequently, a silica upper cladding was deposited to encapsule the Si_3N_4 waveguides via multi-step low-temperature oxide deposition at 400 °C. This was achieved through a low-rate deposition of a liner, followed by the filling of the silica layer using high-density plasma enhanced chemical vapor deposition (HD-PECVD). Finally, we employed lithography and dry etching to create windows on the silica cladding extending to the top surface of the Si_3N_4 waveguides.

Synthesis and coating of GO films. Before GO film coating, a GO solution with small GO flack size (< 100 nm) was prepared by using a modified Hummers method followed by vigorous sonication via a Branson Digital Sonifier[62]. The coating of 2D layered GO films was then achieved by using a transfer-free method that allows for layer-by-layer GO film deposition with precise control of the film thickness, as we did previously[171,172]. During the coating process, four steps for in-situ assembly of monolayer GO films were repeated to construct multi-layered films on the fabricated Si_3N_4 chips with opened windows, including (i) immerse substrate into a 2.0% (w/v) aqueous PDDA (Sigma-Aldrich) solution; (ii) rinse with a stream of deionized distilled water and dry with N_2; (iii) immerse the PDDA-

Preprints (www.preprints.org) | NOT PEER-REVIEWED | Posted: 2 May 2023 doi:10.20944/preprints202305.0082.v1

coated substrate into GO solution; and (iv) rinse with a stream of deionized water and dry with N_2. After the film coating, the chip was dried in a drying oven.

Extracting parametric gain from the measured optical spectra. We used the same methods as those in Refs. [11,43] to extract the signal parametric gain from the measured optical spectra we obtained through OPA experiments. The peak power of the pulsed signal after propagation through the fabricated devices was derived from the measured output optical spectra according to:

$$P_{signal,\,peak} = \frac{\iint P_{signal,\,out}(\lambda)d\lambda}{f_{rep} \times T} \quad (2)$$

where $P_{signal,\,out}(\lambda)$ is the average output power spectrum of the signal as a function of wavelength λ, f_{rep} is the repetition rate of the FPL, and T is the pulse width. In our calculation of $P_{signal,\,peak}$, the power residing in the CW signal line was subtracted from the spectrum of $P_{signal,\,out}(\lambda)$.

After deriving $P_{signal,\,peak}$, the signal parametric gain PG was calculated as:

$$PG\ (\mathrm{dB}) = 10 \times \log_{10}(P_{signal,\,peak} / P_{signal}) \quad (3)$$

where P_{signal} is the CW signal power at the input of the waveguide. According to **Eq. (3)**, the PG in our discussion is the net gain over and above the waveguide loss (including that induced by both the Si_3N_4 waveguide and the GO film). In contrast, the on/off parametric gain is defined as[11,43]

$$PG_{on\text{-}off}\ (\mathrm{dB}) = 10 \times \log_{10}(P_{signal,\,peak} / P_{signal,\,out}) \quad (4)$$

where $P_{signal,out}$ is the CW signal power at the output of the waveguide when the pump is turned off. The parametric gain calculated using **Eq. (4)** is higher than that calculated using **Eq. (3)** since $P_{signal,out}$ is lower than P_{signal}.

OPA Modeling. The third-order optical parametric process in the GO-coated Si_3N_4 waveguides was modeled based on the theory from Refs.[10,58,70]. Assuming negligible depletion of the pump and signal powers due to the generation of the idler, and considering only the short wavelength idler, the coupled differential equations for the dominant degenerate FWM process can be given by[10,65]

$$\frac{dA_p(z)}{dz} = -\frac{\alpha_p}{2}A_p(z) + j\gamma_p\left[|A_p(z)|^2 + 2|A_s(z)|^2 + 2|A_i(z)|^2\right]A_p(z) + j2\gamma_p A_p^*(z)A_s(z)A_i(z)exp(j\Delta\beta z) \quad (5)$$

$$\frac{dA_s(z)}{dz} = -\frac{\alpha_s}{2}A_s(z) + j\gamma_s\left[|A_s(z)|^2 + 2|A_p(z)|^2 + 2|A_i(z)|^2\right]A_s(z) + j\gamma_s A_i^*(z)A_p^2(z)exp(-j\Delta\beta z) \quad (6)$$

$$\frac{dA_i(z)}{dz} = -\frac{\alpha_i}{2}A_i(z) + j\gamma_i\left[|A_i(z)|^2 + 2|A_p(z)|^2 + 2|A_s(z)|^2\right]A_i(z) + j\gamma_i A_s^*(z)A_p^2(z)exp(-j\Delta\beta z) \quad (7)$$

where $A_{p,s,i}$ are the amplitudes of the pump, signal and idler waves along the z axis, which is defined as the light propagation direction, $\alpha_{p,s,i}$ are the loss factor including both the linear loss and the SA-induced nonlinear loss, $\Delta\beta = \beta_s + \beta_i - 2\beta_p$ is the linear phase mismatch, with $\beta_{p,s,i}$ denoting the propagation constants of the pump, signal and idler waves, and $\gamma_{p,s,i}$ are the waveguide nonlinear parameters. In our case, where the wavelength detuning range was small (≤ 10 nm), the linear loss and the nonlinear parameter are assumed to be constant, i.e., $\alpha_p = \alpha_s = \alpha_i = \alpha$, $\gamma_p = \gamma_s = \gamma_i = \gamma$.

In **Eqs. (5) – (7)**, the dispersions $\beta_{p,s,i}$ were calculated via commercial mode solving software using the refractive index n of layered GO films measured by spectral ellipsometry. Given that the photo-thermal changes are sensitive to the average power in the hybrid waveguides, which was below 2 mW for the femtosecond optical pulses studied here, they were considered negligible. By numerically solving **Eqs. (5) – (7)**, the PG was calculated via

$$PG\ (\mathrm{dB}) = 10 \times \log_{10}[|A_s(L)|^2 / |A_s(0)|^2] \quad (8)$$

where L is the length of the Si_3N_4 waveguide (i.e., 20 mm). For our devices with patterned GO films, the waveguides were divided into uncoated Si_3N_4 (without GO films) and hybrid (with GO films) segments with different α, γ and $\beta_{p,s,i}$. The differential equations were solved for each segment, with the output from the previous segment as the input for the subsequent segment.

Extracting n_2 of GO films. The Kerr coefficient n_2 of the layered GO films is extracted from the nonlinear parameter γ of the hybrid waveguides according to:[56,70]

$$\gamma = \frac{2\pi}{\lambda_c} \frac{\iint_D n_0^2(x,y) n_2(x,y) S_z^2 dxdy}{\left[\iint_D n_0(x,y) S_z dxdy\right]^2} \quad (9)$$

where λ_c is the pulse central wavelength, D is the integral of the optical fields over the material regions, S_z is the time-averaged Poynting vector calculated using Lumerical FDTD commercial mode solving software, $n_0(x,y)$ and $n_2(x,y)$ are the linear refractive index and n_2 profiles over the waveguide cross section, respectively. The values of n_2 for silica and Si_3N_4 used in our calculation were 2.60×10^{-20} m^2/W[36] and 2.62×10^{-19} m^2/W, respectively, the latter obtained by fitting the experimental results for the uncoated Si_3N_4 waveguide.

Conflict of Interest: The authors declare no competing financial interest.

References

1. Riemensberger, J. *et al.* A photonic integrated continuous-travelling-wave parametric amplifier. *Nature* **612**, 56-61, doi:10.1038/s41586-022-05329-1 (2022).
2. Liu, Y. *et al.* A photonic integrated circuit–based erbium-doped amplifier. *Science* **376**, 1309-1313, doi:10.1126/science.abo2631 (2022).
3. Foster, M. A. *et al.* Broad-band optical parametric gain on a silicon photonic chip. *Nature* **441**, 960-963, doi:10.1038/nature04932 (2006).
4. Desurvire, E., Simpson, J. R. & Becker, P. C. High-gain erbium-doped traveling-wave fiber amplifier. *Opt. Lett.* **12**, 888-890, doi:10.1364/OL.12.000888 (1987).
5. Temprana, E. *et al.* Overcoming Kerr-induced capacity limit in optical fiber transmission. *Science* **348**, 1445-1448, doi:10.1126/science.aab1781 (2015).
6. Barnard, C., Myslinski, P., Chrostowski, J. & Kavehrad, M. Analytical model for rare-earth-doped fiber amplifiers and lasers. *IEEE J. Quantum Electron.* **30**, 1817-1830, doi:10.1109/3.301646 (1994).
7. Stubkjaer, K. E. Semiconductor optical amplifier-based all-optical gates for high-speed optical processing. *IEEE J. Sel. Top. Quantum Electron.* **6**, 1428-1435, doi:10.1109/2944.902198 (2000).
8. Durhuus, T., Mikkelsen, B., Joergensen, C., Danielsen, S. L. & Stubkjaer, K. E. All-optical wavelength conversion by semiconductor optical amplifiers. *J. Lightwave Technol.* **14**, 942-954, doi:10.1109/50.511594 (1996).
9. Haq, B. *et al.* Micro-Transfer-Printed III-V-on-Silicon C-Band Semiconductor Optical Amplifiers. *Laser Photonics Rev.* **14**, 1900364, doi:https://doi.org/10.1002/lpor.201900364 (2020).
10. Hansryd, J., Andrekson, P. A., Westlund, M., Li, J. & Hedekvist, P. O. Fiber-based optical parametric amplifiers and their applications. *IEEE J. Sel. Top. Quantum Electron.* **8**, 506-520, doi: 10.1109/Jstqe.2002.1016354 (2002).
11. Liu, X., Osgood, R. M., Vlasov, Y. A. & Green, W. M. J. Mid-infrared optical parametric amplifier using silicon nanophotonic waveguides. *Nat. Photonics* **4**, 557-560, doi:10.1038/nphoton.2010.119 (2010).
12. Wu, J., Lin, H., Moss, D. J., Loh, K. P. & Jia, B. Graphene oxide for photonics, electronics and optoelectronics. *Nature Reviews Chemistry* **7** (3) 162–183 (2023). doi:10.1038/s41570-022-00458-7
13. Marhic, M. E. *et al.* Fiber optical parametric amplifiers in optical communication systems. *Laser Photon Rev* **9**, 50-74, doi:10.1002/lpor.201400087 (2015).
14. Wang, C. C. & Racette, G. W. Measurement of parametric gain accompanying optical difference frequency generation. *Appl. Phys. Lett.* **6**, 169-171, doi:10.1063/1.1754219 (1965).
15. Suh, M.-G., Yang, Q.-F., Yang Ki, Y., Yi, X. & Vahala Kerry, J. Microresonator soliton dual-comb spectroscopy. *Science* **354**, 600-603, doi:10.1126/science.aah6516 (2016).
16. Yang, Q.-F. *et al.* Vernier spectrometer using counterpropagating soliton microcombs. *Science* **363**, 965-968, doi:10.1126/science.aaw2317 (2019).
17. Xuanke, Z. *et al.* High-spatial-resolution ultrafast framing imaging at 15 trillion frames per second by optical parametric amplification. *Advanced Photonics* **2**, 056002, doi:10.1117/1.AP.2.5.056002 (2020).
18. Vaughan, P. M. & Trebino, R. Optical-parametric-amplification imaging of complex objects. *Opt. Express* **19**, 8920-8929, doi:10.1364/OE.19.008920 (2011).
19. Linnan Jia, Jiayang Wu, Yuning Zhang, Yang Qu, Baohua Jia, Zhigang Chen, and David J. Moss, "Fabrication Technologies for the On-Chip Integration of 2D Materials", Small: Methods Vol. 6, 2101435 (2022). DOI:10.1002/smtd.202101435.
20. El-Kady, M. F., Strong, V., Dubin, S. & Kaner, R. B. Laser Scribing of High-Performance and Flexible Graphene-Based Electrochemical Capacitors. *Science* **335**, 1326, doi:10.1126/science.1216744 (2012).
21. Reimer, C. *et al.* Generation of multiphoton entangled quantum states by means of integrated frequency combs. *Science* **351**, 1176-1180 (2016). doi:10.1126/science.aad8532

22. Kues, M. *et al.* On-chip generation of high-dimensional entangled quantum states and their coherent control. *Nature* **546**, 622-626 (2017). doi:10.1038/nature22986
23. Del'Haye, P. *et al.* Optical frequency comb generation from a monolithic microresonator. *Nature* **450**, 1214-1217, doi:10.1038/nature06401 (2007).
24. Sun, Y. *et al.* Applications of optical microcombs. *Advances in Optics and Photonics* **15**, 86, (2023). doi:10.1364/aop.470264
25. Trovatello, C. *et al.* Optical parametric amplification by monolayer transition metal dichalcogenides. *Nat. Photonics* **15**, 6-10, doi:10.1038/s41566-020-00728-0 (2020).
26. Sciarrino, F. *et al.* Experimental sub-Rayleigh resolution by an unseeded high-gain optical parametric amplifier for quantum lithography. *Phys. Rev. A* **77**, 012324, doi:10.1103/PhysRevA.77.012324 (2008).
27. Leuthold, J., Koos, C. & Freude, W. Nonlinear silicon photonics. *Nat. Photonics* **4**, 535-544, doi:10.1038/nphoton.2010.185 (2010).
28. Boes, A. *et al.* Lithium niobate photonics: Unlocking the electromagnetic spectrum. *Science* **379**, eabj4396, doi:10.1126/science.abj4396 (2023).
29. Baumgartner, R. & Byer, R. Optical parametric amplification. *IEEE J. Quantum Electron.* **15**, 432-444, doi:10.1109/JQE.1979.1070043 (1979).
30. Petrov, V. *et al.* Second harmonic generation and optical parametric amplification in the mid-IR with orthorhombic biaxial crystals LiGaS2 and LiGaSe2. *Appl. Phys. B* **78**, 543-546, doi:10.1007/s00340-004-1463-0 (2004).
31. Schmidt, B. E. *et al.* Frequency domain optical parametric amplification. *Nat. Commun.* **5**, 3643, doi:10.1038/ncomms4643 (2014).
32. Marhic, M. E., Kagi, N., Chiang, T. K. & Kazovsky, L. G. Broadband fiber optical parametric amplifiers. *Opt. Lett.* **21**, 573-575, doi:10.1364/OL.21.000573 (1996).
33. Marhic, M. E., Wong, K. K. Y. & Kazovsky, L. G. Wide-band tuning of the gain spectra of one-pump fiber optical parametric amplifiers. *IEEE J. Sel. Top. Quantum Electron.* **10**, 1133-1141, doi:10.1109/JSTQE.2004.835298 (2004).
34. Razzari, L. *et al.* CMOS-compatible integrated optical hyper-parametric oscillator. *Nat. Photonics* **4**, 41-45, (2009). doi:10.1038/nphoton.2009.236
35. Pasquazi, A. *et al.* Efficient wavelength conversion and net parametric gain via Four Wave Mixing in a high index doped silica waveguide. *Opt. Express* **18**, 7634-7641 (2010). doi:10.1364/Oe.18.007634
36. Moss, D. J., Morandotti, R., Gaeta, A. L. & Lipson, M. New CMOS-compatible platforms based on silicon nitride and Hydex for nonlinear optics. *Nature Photonics* **7**, 597-607 (2013). doi:10.1038/nphoton.2013.183
37. Arianfard, H., Juodkazis, S., Moss, D. J. & Wu, J. Sagnac interference in integrated photonics. *Applied Physics Reviews* **10**, 011309, doi:10.1063/5.0123236 (2023).
38. Wu, J. *et al.* Graphene Oxide for Integrated Photonics and Flat Optics. *Advanced Materials* **33**, 2006415 (2021). doi:https://doi.org/10.1002/adma.202006415
39. Wu, J. *et al.* RF Photonics: An Optical Microcombs' Perspective. *IEEE J. Sel. Top. Quantum Electron.* **24**, 1-20, (2018). doi:10.1109/jstqe.2018.2805814
40. Wu, J. *et al.* Compact on-chip 1 × 2 wavelength selective switch based on silicon microring resonator with nested pairs of subrings. *Photonics Res.* **3**, 9, doi:10.1364/prj.3.000009 (2014).
41. Liu, J. *et al.* Photonic microwave generation in the X- and K-band using integrated soliton microcombs. *Nat. Photonics* **14**, 486-491, doi:10.1038/s41566-020-0617-x (2020).
42. Wang, T. *et al.* Supercontinuum generation in bandgap engineered, back-end CMOS compatible silicon rich nitride waveguides. *Laser Photonics Rev.* **9**, 498-506, doi:10.1002/lpor.201500054 (2015).
43. Ooi, K. J. *et al.* Pushing the limits of CMOS optical parametric amplifiers with USRN:Si7N3 above the two-photon absorption edge. *Nat. Commun.* **8**, 13878, doi:10.1038/ncomms13878 (2017).
44. Xu, X. *et al.* 11 TOPS photonic convolutional accelerator for optical neural networks. *Nature* **589**, 44-51, (2021). doi:10.1038/s41586-020-03063-0
45. Chang, L. *et al.* Ultra-efficient frequency comb generation in AlGaAs-on-insulator microresonators. *Nat. Commun.* **11**, 1331, doi:10.1038/s41467-020-15005-5 (2020).
46. Yan, Z. *et al.* An Optical Parametric Amplifier via X(2) in AlGaAs Waveguides. *J. Lightwave Technol.* **40**, 5943-5951, doi:10.1109/JLT.2022.3186551 (2022).
47. Kim, D.-G. *et al.* Universal light-guiding geometry for on-chip resonators having extremely high Q-factor. *Nat. Commun.* **11**, 5933, doi:10.1038/s41467-020-19799-2 (2020).
48. Lamont, M. R. E. *et al.* Net-gain from a parametric amplifier on a chalcogenide optical chip. *Opt. Express* **16**, 20374-20381, doi:10.1364/OE.16.020374 (2008).
49. Wilson, D. J. *et al.* Integrated gallium phosphide nonlinear photonics. *Nat. Photonics* **14**, 57-62, doi:10.1038/s41566-019-0537-9 (2019).
50. Jung, H. *et al.* Tantala Kerr nonlinear integrated photonics. *Optica* **8**, 811, doi:10.1364/optica.411968 (2021).
51. Gu, T. *et al.* Regenerative oscillation and four-wave mixing in graphene optoelectronics. *Nat. Photonics* **6**, 554-559, doi:10.1038/nphoton.2012.147 (2012).

52. Jiang, T. *et al.* Gate-tunable third-order nonlinear optical response of massless Dirac fermions in graphene. *Nat. Photonics* **12**, 430-436, doi:10.1038/s41566-018-0175-7 (2018).
53. Seyler, K. L. *et al.* Electrical control of second-harmonic generation in a WSe2 monolayer transistor. *Nat. Nanotechnol.* **10**, 407-411, doi:10.1038/nnano.2015.73 (2015).
54. Zhang, Y. *et al.* Graphene Oxide for Nonlinear Integrated Photonics. *Laser Photonics Rev.*, 2200512, (2023). doi:10.1002/lpor.202200512
55. Zheng, X., Jia, B., Chen, X. & Gu, M. In situ third-order non-linear responses during laser reduction of graphene oxide thin films towards on-chip non-linear photonic devices. *Adv. Mater.* **26**, 2699-2703, doi:10.1002/adma.201304681 (2014).
56. Wu, J. *et al.* 2D Layered Graphene Oxide Films Integrated with Micro-Ring Resonators for Enhanced Nonlinear Optics. *Small* **16**, 1906563, (2020). doi:https://doi.org/10.1002/smll.201906563
57. Zhang, Y. *et al.* Enhanced Kerr Nonlinearity and Nonlinear Figure of Merit in Silicon Nanowires Integrated with 2D Graphene Oxide Films. *ACS Appl. Mater. Interfaces* **12**, 33094-33103, (2020). doi:10.1021/acsami.0c07852
58. Qu, Y. *et al.* Enhanced Four-Wave Mixing in Silicon Nitride Waveguides Integrated with 2D Layered Graphene Oxide Films. *Advanced Optical Materials* **8**, 2001048, (2020). doi:https://doi.org/10.1002/adom.202001048
59. Zhang, Y. *et al.* Enhanced Supercontinuum Generation in Integrated Waveguides Incorporated with Graphene Oxide Films. *Advanced Materials Technologies*, 2201796, (2023). doi:10.1002/admt.202201796
60. Wu, J. *et al.* Graphene Oxide Waveguide and Micro-Ring Resonator Polarizers. *Laser Photonics Rev.* **13**, 1900056, (2019). doi:https://doi.org/10.1002/lpor.201900056
61. Boyd, R. W. *Nonlinear optics*. (Academic press, 2020).
62. Yang, Y. Y. *et al.* Graphene-Based Multilayered Metamaterials with Phototunable Architecture for on-Chip Photonic Devices. *ACS Photonics* **6**, 1033-1040, doi:10.1021/acsphotonics.9b00060 (2019).
63. Bao, Q. *et al.* Broadband graphene polarizer. *Nat. Photonics* **5**, 411-415, doi:10.1038/nphoton.2011.102 (2011).
64. Lin, H. *et al.* Chalcogenide glass-on-graphene photonics. *Nat. Photonics* **11**, 798-805, doi:10.1038/s41566-017-0033-z (2017).
65. Koos, C. *et al.* All-optical high-speed signal processing with silicon–organic hybrid slot waveguides. *Nat. Photonics* **3**, 216-219, doi:10.1038/nphoton.2009.25 (2009).
66. Demongodin, P. *et al.* Ultrafast saturable absorption dynamics in hybrid graphene/Si3N4 waveguides. *APL Photonics* **4**, 076102, doi:10.1063/1.5094523 (2019).
67. Alexander, K., Savostianova, N. A., Mikhailov, S. A., Kuyken, B. & Van Thourhout, D. Electrically Tunable Optical Nonlinearities in Graphene-Covered SiN Waveguides Characterized by Four-Wave Mixing. *ACS Photonics* **4**, 3039-3044, doi:10.1021/acsphotonics.7b00559 (2017).
68. Qu, Y. *et al.* Photo-Thermal Tuning of Graphene Oxide Coated Integrated Optical Waveguides. *Micromachines* **13**, (2022). doi:10.3390/mi13081194
69. Wang, H. *et al.* CMOS-compatible all-optical modulator based on the saturable absorption of graphene. *Photonics Res.* **8**, 468, doi:10.1364/prj.380170 (2020).
70. Yang, Y. *et al.* Invited Article: Enhanced four-wave mixing in waveguides integrated with graphene oxide. *APL Photonics* **3**, 120803, (2018). doi:10.1063/1.5045509
71. Zhang, Y. *et al.* Enhanced self-phase modulation in silicon nitride waveguides integrated with 2D graphene oxide films. *IEEE J. Sel. Top. Quantum Electronics* **29** (2023). doi:10.1109/jstqe.2022.3177385
72. El Dirani, H. *et al.* Ultralow-loss tightly confining Si3N4 waveguides and high-Q microresonators. *Opt. Express* **27**, 30726-30740, doi:10.1364/OE.27.030726 (2019).
73. Yang Qu, Jiayang Wu, Yuning Zhang, Yunyi Yang, Linnan Jia, Baohua Jia, and David J. Moss, "Photo thermal tuning in GO-coated integrated waveguides", Micromachines Vol. 13 1194 (2022). doi.org/10.3390/mi13081194
74. Yuning Zhang, Jiayang Wu, Yunyi Yang, Yang Qu, Linnan Jia, Baohua Jia, and David J. Moss, "Enhanced spectral broadening of femtosecond optical pulses in silicon nanowires integrated with 2D graphene oxide films", Micromachines Vol. 13 756 (2022). DOI:10.3390/mi13050756.
75. Linnan Jia, Jiayang Wu, Yuning Zhang, Yang Qu, Baohua Jia, Zhigang Chen, and David J. Moss, "Fabrication Technologies for the On-Chip Integration of 2D Materials", Small: Methods 6, 2101435 (2022). DOI:10.1002/smtd.202101435.
76. Yuning Zhang, Jiayang Wu, Yang Qu, Linnan Jia, Baohua Jia, and David J. Moss, "Design and optimization of four-wave mixing in microring resonators integrated with 2D graphene oxide films", Journal of Lightwave Technology 39 (20) 6553-6562 (2021). DOI:10.1109/JLT.2021.3101292. Print ISSN: 0733-8724, Online ISSN: 1558-2213 (2021).
77. Yuning Zhang, Jiayang Wu, Yang Qu, Linnan Jia, Baohua Jia, and David J. Moss, "Optimizing the Kerr nonlinear optical performance of silicon waveguides integrated with 2D graphene oxide films", Journal of Lightwave Technology Vol. 39 (14) 4671-4683 (2021). DOI: 10.1109/JLT.2021.3069733.

78. Yang Qu, Jiayang Wu, Yuning Zhang, Yao Liang, Baohua Jia, and David J. Moss, "Analysis of four-wave mixing in silicon nitride waveguides integrated with 2D layered graphene oxide films", Journal of Lightwave Technology Vol. 39 (9) 2902-2910 (2021). DOI: 10.1109/JLT.2021.3059721.
79. Y. Qu, J. Wu, Y. Zhang, L. Jia, Y. Yang, X. Xu, S. T. Chu, B. E. Little, R. Morandotti, B. Jia, and D. J. Moss, "Graphene oxide for enhanced optical nonlinear performance in CMOS compatible integrated devices", Paper No. 11688-30, PW21O-OE109-36, 2D Photonic Materials and Devices IV, SPIE Photonics West, San Francisco CA March 6-11 (2021). doi.org/10.1117/12.2583978
80. Yuning Zhang, Yang Qu, Jiayang Wu, Linnan Jia, Yunyi Yang, Xingyuan Xu, Baohua Jia, and David J. Moss, "Enhanced Kerr nonlinearity and nonlinear figure of merit in silicon nanowires integrated with 2D graphene oxide films", ACS Applied Materials and Interfaces vol. 12 (29) 33094−33103 June 29 (2020). DOI:10.1021/acsami.0c07852
81. Jiayang Wu, Yunyi Yang, Yang Qu, Xingyuan Xu, Yao Liang, Sai T. Chu, Brent E. Little, Roberto Morandotti, Baohua Jia, and David J. Moss, "Graphene oxide waveguide polarizers and polarization selective micro-ring resonators", Paper 11282-29, SPIE Photonics West, San Francisco, CA, 4 - 7 February (2020). doi: 10.1117/12.2544584
82. Jiayang Wu, Yunyi Yang, Yang Qu, Xingyuan Xu, Yao Liang, Sai T. Chu, Brent E. Little, Roberto Morandotti, Baohua Jia, and David J. Moss, "Graphene oxide waveguide polarizers and polarization selective micro-ring resonators", Laser and Photonics Reviews vol. 13 (9) 1900056 (2019). DOI:10.1002/lpor.201900056.
83. Xu, X., et al., Photonic microwave true time delays for phased array antennas using a 49 GHz FSR integrated micro-comb source, Photonics Research, 6, B30-B36 (2018).
84. X. Xu, M. Tan, J. Wu, R. Morandotti, A. Mitchell, and D. J. Moss, "Microcomb-based photonic RF signal processing", IEEE Photonics Technology Letters, vol. 31 no. 23 1854-1857, 2019.
85. M. Tan et al, "Orthogonally polarized Photonic Radio Frequency single sideband generation with integrated micro-ring resonators", IOP Journal of Semiconductors, Vol. 42 (4), 041305 (2021). DOI: 10.1088/1674-4926/42/4/041305.
86. Mengxi Tan, X. Xu, J. Wu, T. G. Nguyen, S. T. Chu, B. E. Little, R. Morandotti, A. Mitchell, and David J. Moss, "Photonic Radio Frequency Channelizers based on Kerr Optical Micro-combs", IOP Journal of Semiconductors Vol. 42 (4), 041302 (2021). DOI:10.1088/1674-4926/42/4/041302.
87. Xu, et al., "Advanced adaptive photonic RF filters with 80 taps based on an integrated optical micro-comb source," Journal of Lightwave Technology, vol. 37, no. 4, pp. 1288-1295 (2019).
88. X. Xu, et al., Broadband microwave frequency conversion based on an integrated optical micro-comb source", Journal of Lightwave Technology, vol. 38 no. 2, pp. 332-338, 2020.
89. M. Tan, et al., "Photonic RF and microwave filters based on 49GHz and 200GHz Kerr microcombs", Optics Comm. vol. 465,125563, Feb. 22. 2020.
90. X. Xu, et al., "Broadband photonic RF channelizer with 90 channels based on a soliton crystal microcomb", Journal of Lightwave Technology, Vol. 38, no. 18, pp. 5116 - 5121, 2020. doi: 10.1109/JLT.2020.2997699.
91. X. Xu, et al., "Photonic RF and microwave integrator with soliton crystal microcombs", IEEE Transactions on Circuits and Systems II: Express Briefs, vol. 67, no. 12, pp. 3582-3586, 2020. DOI:10.1109/TCSII.2020.2995682.
92. X. Xu, et al., "High performance RF filters via bandwidth scaling with Kerr micro-combs," APL Photonics, vol. 4 (2) 026102. 2019.
93. M. Tan, et al., "Microwave and RF photonic fractional Hilbert transformer based on a 50 GHz Kerr micro-comb", Journal of Lightwave Technology, vol. 37, no. 24, pp. 6097 – 6104, 2019.
94. M. Tan, et al., "RF and microwave fractional differentiator based on photonics", IEEE Transactions on Circuits and Systems: Express Briefs, vol. 67, no.11, pp. 2767-2771, 2020. DOI:10.1109/TCSII.2020.2965158.
95. M. Tan, et al., "Photonic RF arbitrary waveform generator based on a soliton crystal micro-comb source", Journal of Lightwave Technology, vol. 38, no. 22, pp. 6221-6226 (2020). DOI: 10.1109/JLT.2020.3009655.
96. M. Tan, X. Xu, J. Wu, R. Morandotti, A. Mitchell, and D. J. Moss, "RF and microwave high bandwidth signal processing based on Kerr Micro-combs", Advances in Physics X, VOL. 6, NO. 1, 1838946 (2021). DOI:10.1080/23746149.2020.1838946.
97. X. Xu, et al., "Advanced RF and microwave functions based on an integrated optical frequency comb source," Opt. Express, vol. 26 (3) 2569 (2018).
98. M. Tan, X. Xu, J. Wu, B. Corcoran, A. Boes, T. G. Nguyen, S. T. Chu, B. E. Little, R.Morandotti, A. Lowery, A. Mitchell, and D. J. Moss, ""Highly Versatile Broadband RF Photonic Fractional Hilbert Transformer Based on a Kerr Soliton Crystal Microcomb", Journal of Lightwave Technology vol. 39 (24) 7581-7587 (2021).
99. Wu, J. et al. RF Photonics: An Optical Microcombs' Perspective. IEEE Journal of Selected Topics in Quantum Electronics Vol. 24, 6101020, 1-20 (2018).
100. T. G. Nguyen et al., "Integrated frequency comb source-based Hilbert transformer for wideband microwave photonic phase analysis," Opt. Express, vol. 23, no. 17, pp. 22087-22097, Aug. 2015.

101. X. Xu, J. Wu, M. Shoeiby, T. G. Nguyen, S. T. Chu, B. E. Little, R. Morandotti, A. Mitchell, and D. J. Moss, "Reconfigurable broadband microwave photonic intensity differentiator based on an integrated optical frequency comb source," APL Photonics, vol. 2, no. 9, 096104, Sep. 2017.
102. X. Xu, et al., "Broadband RF channelizer based on an integrated optical frequency Kerr comb source," Journal of Lightwave Technology, vol. 36, no. 19, pp. 4519-4526, 2018.
103. X. Xu, et al., "Continuously tunable orthogonally polarized RF optical single sideband generator based on micro-ring resonators," Journal of Optics, vol. 20, no. 11, 115701. 2018.
104. X. Xu, et al., "Orthogonally polarized RF optical single sideband generation and dual-channel equalization based on an integrated microring resonator," Journal of Lightwave Technology, vol. 36, no. 20, pp. 4808-4818. 2018.
105. X. Xu, et al., "Photonic RF phase-encoded signal generation with a microcomb source", J. Lightwave Technology, vol. 38, no. 7, 1722-1727, 2020.
106. B. Corcoran, et al., "Ultra-dense optical data transmission over standard fiber with a single chip source", Nature Communications, vol. 11, Article:2568, 2020.
107. X. Xu et al, "Photonic perceptron based on a Kerr microcomb for scalable high speed optical neural networks", Laser and Photonics Reviews, vol. 14, no. 8, 2000070 (2020). DOI: 10.1002/lpor.202000070.
108. X. Xu, et al., "11 TOPs photonic convolutional accelerator for optical neural networks", Nature 589, 44-51 (2021).
109. X. Xu et al., "Neuromorphic computing based on wavelength-division multiplexing", Vol. 28 IEEE Journal of Selected Topics in Quantum Electronics Vol. 29 Issue: 2, Article 7400112 (2023). DOI:10.1109/JSTQE.2022.3203159.
110. Yang Sun, Jiayang Wu, Mengxi Tan, Xingyuan Xu, Yang Li, Roberto Morandotti, Arnan Mitchell, and David Moss, "Applications of optical micro-combs", Advances in Optics and Photonics Vol. 15 (1) 86-175 (2023). DOI:10.1364/AOP.470264.
111. Yunping Bai, Xingyuan Xu,1, Mengxi Tan, Yang Sun, Yang Li, Jiayang Wu, Roberto Morandotti, Arnan Mitchell, Kun Xu, and David J. Moss, "Photonic multiplexing techniques for neuromorphic computing", Nanophotonics Vol. 12 (5): 795–817 (2023). DOI:10.1515/nanoph-2022-0485.
112. Chawaphon Prayoonyong, Andreas Boes, Xingyuan Xu, Mengxi Tan, Sai T. Chu, Brent E. Little, Roberto Morandotti, Arnan Mitchell, David J. Moss, and Bill Corcoran, "Frequency comb distillation for optical superchannel transmission", Journal of Lightwave Technology Vol. 39 (23) 7383-7392 (2021). DOI: 10.1109/JLT.2021.3116614.
113. Mengxi Tan, Xingyuan Xu, Jiayang Wu, Bill Corcoran, Andreas Boes, Thach G. Nguyen, Sai T. Chu, Brent E. Little, Roberto Morandotti, Arnan Mitchell, and David J. Moss, "Integral order photonic RF signal processors based on a soliton crystal micro-comb source", IOP Journal of Optics Vol. 23 (11) 125701 (2021). https://doi.org/10.1088/2040-8986/ac2eab
114. Yang Sun, Jiayang Wu, Yang Li, Xingyuan Xu, Guanghui Ren, Mengxi Tan, Sai Tak Chu, Brent E. Little, Roberto Morandotti, Arnan Mitchell, and David J. Moss, "Performance analysis of microcomb-based microwave photonic transversal signal processors with experimental errors", Journal of Lightwave Technology 41 Special Issue on Microwave Photonics (2023).
115. Yang Sun, Jiayang Wu, Yang Li, Mengxi Tan, Xingyuan Xu, Sai Chu, Brent Little, Roberto Morandotti, Arnan Mitchell, and David J. Moss, "Quantifying the Accuracy of Microcomb-based Photonic RF Transversal Signal Processors", IEEE Journal of Selected Topics in Quantum Electronics 29 (2023). DOI: 10.1109/JSTQE.2023.3266276.
116. Mengxi Tan, Xingyuan Xu, Andreas Boes, Bill Corcoran, Thach G. Nguyen, Sai T. Chu, Brent E. Little, Roberto Morandotti, Jiayang Wu, Arnan Mitchell, and David J. Moss, "Photonic signal processor for real-time video image processing at 17 Tb/s", Communications Engineering 2 (2023). Reference research square
117. A. Pasquazi, et al., "Sub-picosecond phase-sensitive optical pulse characterization on a chip", Nature Photonics, vol. 5, no. 10, pp. 618-623 (2011).
118. Bao, C., et al., Direct soliton generation in microresonators, Opt. Lett, 42, 2519 (2017).
119. M.Ferrera et al., "CMOS compatible integrated all-optical RF spectrum analyzer", Optics Express, vol. 22, no. 18, 21488 - 21498 (2014).
120. M. Kues, et al., "Passively modelocked laser with an ultra-narrow spectral width", Nature Photonics, vol. 11, no. 3, pp. 159, 2017.
121. L. Razzari, et al., "CMOS-compatible integrated optical hyper-parametric oscillator," Nature Photonics, vol. 4, no. 1, pp. 41-45, 2010.
122. M. Ferrera, et al., "Low-power continuous-wave nonlinear optics in doped silica glass integrated waveguide structures," Nature Photonics, vol. 2, no. 12, pp. 737-740, 2008.
123. M.Ferrera et al."On-Chip ultra-fast 1st and 2nd order CMOS compatible all-optical integration", Opt. Express, vol. 19, (23)pp. 23153-23161 (2011).
124. D. Duchesne, M. Peccianti, M. R. E. Lamont, et al., "Supercontinuum generation in a high index doped silica glass spiral waveguide," Optics Express, vol. 18, no, 2, pp. 923-930, 2010.

125. H Bao, L Olivieri, M Rowley, ST Chu, BE Little, R Morandotti, DJ Moss, ... "Turing patterns in a fiber laser with a nested microresonator: Robust and controllable microcomb generation", Physical Review Research 2 (2), 023395 (2020).
126. M. Ferrera, et al., "On-chip CMOS-compatible all-optical integrator", Nature Communications, vol. 1, Article 29, 2010.
127. A. Pasquazi, et al., "All-optical wavelength conversion in an integrated ring resonator," Optics Express, vol. 18, no. 4, pp. 3858-3863, 2010.
128. A.Pasquazi, Y. Park, J. Azana, et al., "Efficient wavelength conversion and net parametric gain via Four Wave Mixing in a high index doped silica waveguide," Optics Express, vol. 18, no. 8, pp. 7634-7641, 2010.
129. M. Peccianti, M. Ferrera, L. Razzari, et al., "Subpicosecond optical pulse compression via an integrated nonlinear chirper," Optics Express, vol. 18, no. 8, pp. 7625-7633, 2010.
130. M. Ferrera et al., "Low Power CW Parametric Mixing in a Low Dispersion High Index Doped Silica Glass Micro-Ring Resonator with Q-factor > 1 Million", Optics Express, vol.17, no. 16, pp. 14098–14103 (2009).
131. M. Peccianti, et al., "Demonstration of an ultrafast nonlinear microcavity modelocked laser", Nature Communications, vol. 3, pp. 765, 2012.
132. A.Pasquazi, et al., "Self-locked optical parametric oscillation in a CMOS compatible microring resonator: a route to robust optical frequency comb generation on a chip," Optics Express, vol. 21, no. 11, pp. 13333-13341, 2013.
133. A.Pasquazi, et al., "Stable, dual mode, high repetition rate mode-locked laser based on a microring resonator," Optics Express, vol. 20, no. 24, pp. 27355-27362, 2012.
134. Pasquazi, A. et al. Micro-combs: a novel generation of optical sources. Physics Reports 729, 1-81 (2018).
135. Moss, D. J. et al., "New CMOS-compatible platforms based on silicon nitride and Hydex for nonlinear optics", Nature photonics 7, 597 (2013).
136. H. Bao, et al., Laser cavity-soliton microcombs, Nature Photonics, vol. 13, no. 6, pp. 384-389, Jun. 2019.
137. Antonio Cutrona, Maxwell Rowley, Debayan Das, Luana Olivieri, Luke Peters, Sai T. Chu, Brent L. Little, Roberto Morandotti, David J. Moss, Juan Sebastian Totero Gongora, Marco Peccianti, Alessia Pasquazi, "High Conversion Efficiency in Laser Cavity-Soliton Microcombs", Optics Express Vol. 30, Issue 22, pp. 39816-39825 (2022). https://doi.org/10.1364/OE.470376.
138. M.Rowley, P.Hanzard, A.Cutrona, H.Bao, S.Chu, B.Little, R.Morandotti, D. J. Moss, G. Oppo, J. Gongora, M. Peccianti and A. Pasquazi, "Self-emergence of robust solitons in a micro-cavity", Nature 608 (7922) 303–309 (2022).
139. Hamed Arianfard, Saulius Juodkazis, David J. Moss, and Jiayang Wu, "Sagnac interference in integrated photonics", Applied Physics Reviews vol. 10 (1) 011309 (2023). doi: 10.1063/5.0123236. (2023).
140. Linnan Jia, Yang Qu, Jiayang Wu, Yuning Zhang, Yunyi Yang, Baohua Jia, and David J. Moss, "Third-order optical nonlinearities of 2D materials at telecommunications wavelengths", Micromachines (MDPI), 14, 307 (2023). https://doi.org/10.3390/mi14020307.
141. Hamed Arianfard, Jiayang Wu, Saulius Juodkazis, and David J. Moss, "Optical analogs of Rabi splitting in integrated waveguide-coupled resonators", Advanced Physics Research 2 (2023). DOI: 10.1002/apxr.202200123.
142. Hamed Arianfard, Jiayang Wu, Saulius Juodkazis, and David J. Moss, "Spectral shaping based on optical waveguides with advanced Sagnac loop reflectors", Paper No. PW22O-OE201-20, SPIE-Opto, Integrated Optics: Devices, Materials, and Technologies XXVI, SPIE Photonics West, San Francisco CA January 22 - 27 (2022). doi: 10.1117/12.2607902
143. Hamed Arianfard, Jiayang Wu, Saulius Juodkazis, David J. Moss, "Spectral Shaping Based on Integrated Coupled Sagnac Loop Reflectors Formed by a Self-Coupled Wire Waveguide", IEEE Photonics Technology Letters vol. 33 (13) 680-683 (2021). DOI:10.1109/LPT.2021.3088089.
144. Hamed Arianfard, Jiayang Wu, Saulius Juodkazis and David J. Moss, "Three Waveguide Coupled Sagnac Loop Reflectors for Advanced Spectral Engineering", Journal of Lightwave Technology vol. 39 (11) 3478-3487 (2021). DOI: 10.1109/JLT.2021.3066256.
145. Hamed Arianfard, Jiayang Wu, Saulius Juodkazis and David J. Moss, "Advanced Multi-Functional Integrated Photonic Filters based on Coupled Sagnac Loop Reflectors", Journal of Lightwave Technology vol. 39 Issue: 5, pp.1400-1408 (2021). DOI:10.1109/JLT.2020.3037559.
146. Hamed Arianfard, Jiayang Wu, Saulius Juodkazis and David J. Moss, "Advanced multi-functional integrated photonic filters based on coupled Sagnac loop reflectors", Paper 11691-4, PW21O-OE203-44, Silicon Photonics XVI, SPIE Photonics West, San Francisco CA March 6-11 (2021). doi.org/10.1117/12.2584020
147. Jiayang Wu, Tania Moein, Xingyuan Xu, and David J. Moss, "Advanced photonic filters via cascaded Sagnac loop reflector resonators in silicon-on-insulator integrated nanowires", Applied Physics Letters Photonics vol. 3 046102 (2018). DOI:/10.1063/1.5025833

148. Jiayang Wu, Tania Moein, Xingyuan Xu, Guanghui Ren, Arnan Mitchell, and David J. Moss, "Micro-ring resonator quality factor enhancement via an integrated Fabry-Perot cavity", Applied Physics Letters Photonics vol. 2 056103 (2017). doi: 10.1063/1.4981392.
149. Linnan Jia, Dandan Cui, Jiayang Wu, Haifeng Feng, Tieshan Yang, Yunyi Yang, Yi Du, Weichang Hao, Baohua Jia, David J. Moss, "BiOBr nanoflakes with strong nonlinear optical properties towards hybrid integrated photonic devices", Applied Physics Letters Photonics vol. 4 090802 (2019). DOI: 10.1063/1.5116621
150. Linnan Jia, Jiayang Wu, Yunyi Yang, Yi Du, Baohua Jia, David J. Moss, "Large Third-Order Optical Kerr Nonlinearity in Nanometer-Thick PdSe2 2D Dichalcogenide Films: Implications for Nonlinear Photonic Devices", ACS Applied Nano Materials vol. 3 (7) 6876–6883 (2020). DOI:10.1021/acsanm.0c01239.
151. E.D Ghahramani, DJ Moss, JE Sipe, "Full-band-structure calculation of first-, second-, and third-harmonic optical response coefficients of ZnSe, ZnTe, and CdTe", Physical Review B 43 (12), 9700 (1991).
152. C Grillet, C Smith, D Freeman, S Madden, B Luther-Davies, EC Magi, ... "Efficient coupling to chalcogenide glass photonic crystal waveguides via silica optical fiber nanowires", Optics Express vol. 14 (3), 1070-1078 (2006).
153. S Tomljenovic-Hanic, MJ Steel, CM de Sterke, DJ Moss, "High-Q cavities in photosensitive photonic crystals" Optics Letters vol. 32 (5), 542-544 (2007).
154. M Ferrera et al., "On-Chip ultra-fast 1st and 2nd order CMOS compatible all-optical integration", Optics Express vol. 19 (23), 23153-23161 (2011).
155. VG Ta'eed et al., "Error free all optical wavelength conversion in highly nonlinear As-Se chalcogenide glass fiber", Optics Express vol. 14 (22), 10371-10376 (2006).
156. M Rochette, L Fu, V Ta'eed, DJ Moss, BJ Eggleton, "2R optical regeneration: an all-optical solution for BER improvement", IEEE Journal of Selected Topics in Quantum Electronics vol. 12 (4), 736-744 (2006).
157. TD Vo, et al., "Silicon-chip-based real-time dispersion monitoring for 640 Gbit/s DPSK signals", Journal of Lightwave Technology vol. 29 (12), 1790-1796 (2011).
158. Kues, M. et al. "Quantum optical microcombs", Nature Photonics 13, (3) 170-179 (2019). doi:10.1038/s41566-019-0363-0
159. C.Reimer, L. Caspani, M. Clerici, et al., "Integrated frequency comb source of heralded single photons," Optics Express, vol. 22, no. 6, pp. 6535-6546, 2014.
160. C.Reimer, et al., "Cross-polarized photon-pair generation and bi-chromatically pumped optical parametric oscillation on a chip", Nature Communications, vol. 6, Article 8236, 2015. DOI: 10.1038/ncomms9236.
161. L. Caspani, C. Reimer, M. Kues, et al., "Multifrequency sources of quantum correlated photon pairs on-chip: a path toward integrated Quantum Frequency Combs," Nanophotonics, vol. 5, no. 2, pp. 351-362, 2016.
162. C. Reimer et al., "Generation of multiphoton entangled quantum states by means of integrated frequency combs," Science, vol. 351, no. 6278, pp. 1176-1180, 2016.
163. M. Kues, et al., "On-chip generation of high-dimensional entangled quantum states and their coherent control", Nature, vol. 546, no. 7660, pp. 622-626, 2017.
164. P. Roztocki et al., "Practical system for the generation of pulsed quantum frequency combs," Optics Express, vol. 25, no. 16, pp. 18940-18949, 2017.
165. Y. Zhang, et al., "Induced photon correlations through superposition of two four-wave mixing processes in integrated cavities", Laser and Photonics Reviews, vol. 14, no. 7, pp. 2000128, 2020. DOI: 10.1002/lpor.202000128
166. C. Reimer, et al., "High-dimensional one-way quantum processing implemented on d-level cluster states", Nature Physics, vol. 15, no.2, pp. 148–153, 2019.
167. P.Roztocki et al., "Complex quantum state generation and coherent control based on integrated frequency combs", Journal of Lightwave Technology 37 (2) 338-347 (2019).
168. S. Sciara et al., "Generation and Processing of Complex Photon States with Quantum Frequency Combs", IEEE Photonics Technology Letters 31 (23) 1862-1865 (2019). DOI: 10.1109/LPT.2019.2944564.
169. Stefania Sciara, Piotr Roztocki, Bennet Fisher, Christian Reimer, Luis Romero Cortez, William J. Munro, David J. Moss, Alfonso C. Cino, Lucia Caspani, Michael Kues, J. Azana, and Roberto Morandotti, "Scalable and effective multilevel entangled photon states: A promising tool to boost quantum technologies", Nanophotonics 10 (18), 4447–4465 (2021). DOI:10.1515/nanoph-2021-0510.
170. L. Caspani, C. Reimer, M. Kues, et al., "Multifrequency sources of quantum correlated photon pairs on-chip: a path toward integrated Quantum Frequency Combs," Nanophotonics, vol. 5, no. 2, pp. 351-362, 2016.
171. Lin, H. *et al.* A 90-nm-thick graphene metamaterial for strong and extremely broadband absorption of unpolarized light. *Nat. Photonics* **13**, 270-276, doi:10.1038/s41566-019-0389-3 (2019).
172. Lin, K. T., Lin, H., Yang, T. & Jia, B. Structured graphene metamaterial selective absorbers for high efficiency and omnidirectional solar thermal energy conversion. *Nat. Commun.* **11**, 1389, doi:10.1038/s41467-020-15116-z (2020).

 doi:10.20944/preprints202305.0082.v1